A Multi-stage Design Approach for Optimizing a PMSG-based Grid-connected Ocean Wave Energy Conversion System

Muhammad Noman, Guojie Li, *Senior Member*, *IEEE*, Muhammad Waseem Khan, Keyou Wang, and Bei Han

***Abstract*—Fully harnessing the ocean wave's renewable energy resources could benefit coastal countries. However, ocean wave energy harvesting systems encounter several challenges, i.e., marine uncertainties, long-distance maintenance, power fluctuations, irregular wave currents, non-linear generator dynamics, turbine limitations, cost optimization, and power smoothing issues. To overcome these challenges, this paper proposes a new multi-stage control design approach for performance evaluation of the oscillating water column (OWC)-based ocean wave energy conversion (OWEC) system. The first stage optimizes the Wells turbine by implementing an efficient airflow control strategy. It achieves maximum power-harvesting ability by eliminating stalling phenomena. In the second stage, we investigate the robustness of the permanent magnet synchronous generator-based OWEC system by designing adaptive back-stepping controllers, taking into account the Lyapunov stability theory. It accomplishes precise speed regulation for optimal power extraction while delivering reduced delay response and percentage errors. To ensure the OWEC system's availability, the third stage incorporates fault-ride-through capabilities. It executes a fault reconfigurable control for a parallel converter configuration, eliminating only the faulty leg instead of the entire power converter. In the fourth stage, a supercapacitors-based energy management system achieves power smoothing, even when the OWC plant output power fluctuates. We accomplish this by implementing a model predictive control strategy. Finally, the Matlab/Simulink results verify that the presented multi-stage control for the OWC OWEC system is an effective design approach, offering an optimal, robust, reliable, and power-smoothing solution.**

***Index Terms*—Ocean wave energy, oscillating water column, Wells turbine, adaptive control, fault-tolerant control, energy management system.**

I. Introduction

Energy is a key factor influencing the characteristics and dynamics of nature's surroundings. The gradual depletion of traditional energy resources has led researchers to seek other forms of renewable energy. Therefore, ocean wave energy has emerged as one of the most prominent technologies within the renewable energy category. The wave energy varies from approximately 8000 TWh to 80 000 TWh per year [1]. On average, each wave crest carries 10 kW to 50 kW per meter, producing a total power output of 1 TW to 10 TW [2]. Despite its significant potential, the current contribution of ocean wave energy to global power generation still needs to be higher. However, several countries have successfully implemented fully operational, commercial, or pilot plants that harness ocean wave energy [3], [4].

An extensive global investigation has recently been conducted on oscillating water column (OWC)-based ocean wave energy conversion (OWEC) systems [3]–[5]. These investigations primarily aim to boost the efficiency of OWC devices. Nevertheless, it is crucial to make significant investments in the renewable energy technology industry to overcome challenges restricting the development of OWEC systems. The novelty of OWC devices is the primary factor contributing to the challenges [6]. It is also essential to control the potential non-linearities, generator response time, and uncertainties that come with permanent magnet synchronous generator (PMSG)-based OWEC systems. Therefore, this paper proposes a novel design approach that focuses on the overall performance evaluation of an OWC OWEC system. Figure 1 illustrates the fundamental aspects of the proposed design approach. This approach is distinctive in its ability to effectively deal with the complicated challenges of providing sustained electrical power from the grid-connected OWC OWEC system. The challenges include high capital and operational costs, marine environment uncertainties, device limitations, power fluctuations, generator non-linear dynamics, power delivery, and long-distance maintenance [7], [8].

Received: December 29, 2023
Accepted: July 5, 2024
Published Online: November 1, 2024

Muhammad Noman, Guojie Li (corresponding author), Keyou Wang, and Bei Han are with the Key Laboratory of Control of Power Transmission and Conversion, Ministry of Education (MOE), the Department of Electrical Engineering, Shanghai Jiao Tong University, Shanghai 200030, China (e-mail: m_noman@sjtu.edu.cn; liguojie@sjtu.edu.cn; wangkeyou@sjtu.edu.cn; han_bei@sjtu.edu.cn).

Muhammad Waseem Khan is with the Interdisciplinary Research Center for Sustainable Energy Systems (IRC-SES), King Fahd University of Petroleum & Minerals, Dhahran 31261, Saudi Arabia (e-mail: engr_waseem90@yahoo.com)

DOI: 10.23919/PCMP.2023.000013

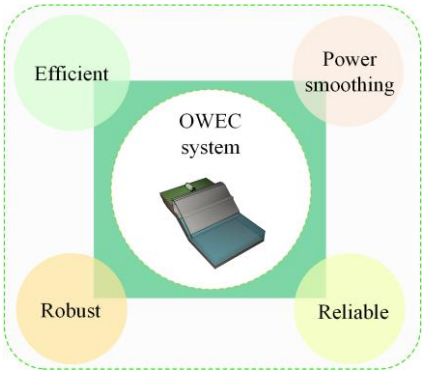

Fig. 1. Fundamental aspects of the proposed approach.

In this paper, the proposed approach involves a four-stage multi-control design to investigate the above-mentioned challenges and incorporate the optimal control stages into the OWC OWEC system, offering an efficient solution. The proposed solution assesses a comprehensive performance improvement by examining uncontrolled and controlled OWC OWEC systems. Thus, the main objective is to streamline optimal control strategies for long-term sustainability of marine renewable energy systems. Figure 2 illustrates the primary objectives of the proposed OWEC system.

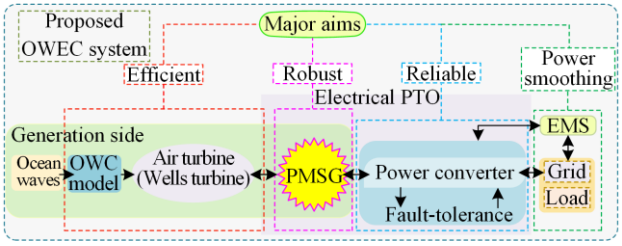

Fig. 2. Proposed multi-stage design methodology.

In order to provide an appropriate context for this research, the contributions can be given as follows.

1) To eliminate the stalling behavior of the Wells turbine under irregular wave scenario, thereby achieving maximum power extraction.

2) To enhance the system's electrical control by implementing a non-linear adaptive back-stepping controller using the Lyapunov stability method.

3) To ensure the OWEC system's reliability by incorporating a multi-leg fault ride-through (FRT) capability based on a parallel power converter topology.

4) To prevent variations and enhance the power quality supplied to the grid side by integrating a model predictive control (MPC)-based energy management system (EMS) that includes supercapacitors (SCs).

Further sections of this paper are organized in the following order. Section II provides a concise overview of the multi-stage solution. Section III implements the OWC device's optimal power extraction scheme and generation-side converter (GSC) control. Section IV provides the FRT capability in a parallel power converter configuration. Section V presents the SC-EMS. Section VI provides a detailed evaluation of the simulated outcomes. Finally, Section VII draws a comprehensive conclusion to this paper.

II. An Overview Of the Multi-Stage Design Approach

This section briefly overviews the proposed multi-stage control design and a comprehensive literature review based on existing control strategies. Figure 3 depicts the overall multi-stage philosophy.

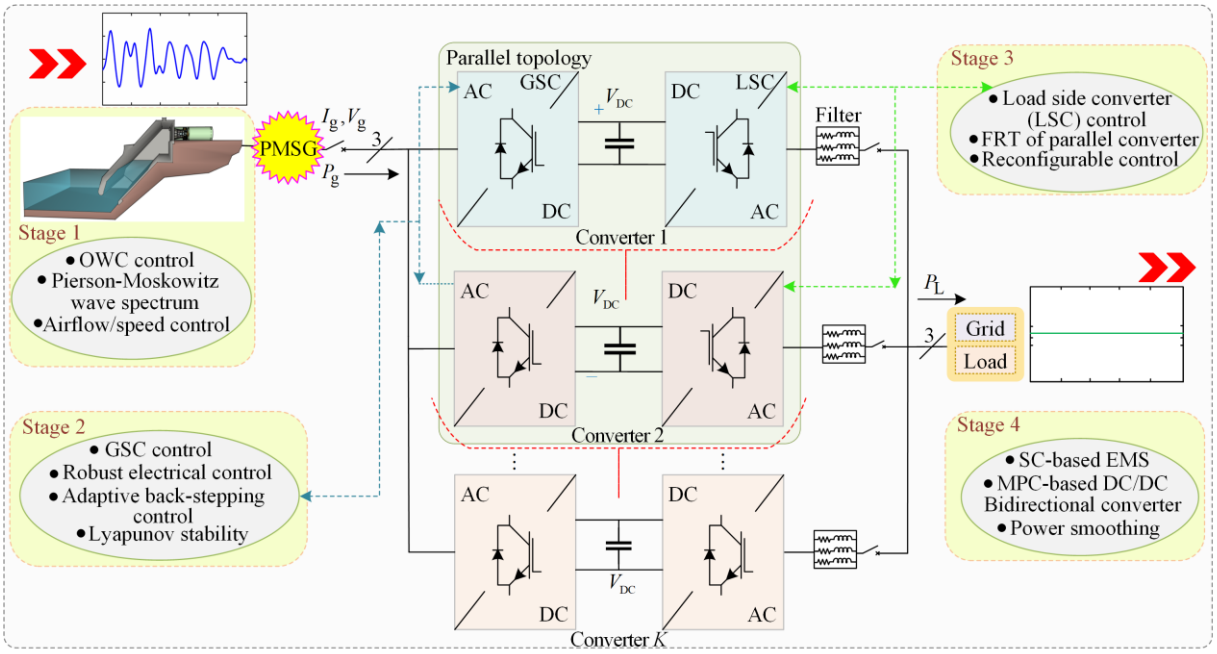

Fig. 3. Illustration of the four-stage design approach.

A. Stage One

To design a cost-effective OWC OWEC system, it is vital to implement control strategies to eliminate the primary power take-off (PTO) mechanism's physical and operational limits. Also, the OWC device's performance enhancement requires careful assessment of several parameters, such as the acceptable range of speeds, the turbine's dynamic constraints, stalling limitations, and the power quality supplied to the grid [9]. In this context, the proposed first-stage solution is critical for implementing the maximum power harnessing scheme to achieve efficient control operations.

To execute optimal power output, we have implemented proportional-integral (PI) and fractional-order proportional integral derivative (FOPID)-based control methods. These controllers are accountable for regulating airflow inside the OWC chamber. The proposed controllers, however, limit the stalling behavior while providing an appropriate pressure drop and oscillations. The implemented PI controller simplifies the open-loop transfer function by considering both the controller and the reference signals. In contrast to a conventional controller, incorporating a FOPID intends to improve the controller's stability in scenarios where the feedback loop remains unchanged by performance parameters while also attempting to decrease the occurrence of errors. Section III will address the modeling of these controllers.

Furthermore, the Pierson-Moskowitz (PM) spectrum based on an actual wave scenario have been considered to investigate the complexity and uncertainty of the OWEC system. Previously, several control strategies have been developed to regulate wave energy converters (WECs) [10]–[13]. A controller utilizing the oscillating rotor blades of the Wells turbine was offered in [10] to enhance the performance of the OWC system. In [11], researchers designed a reactive controller for a fixed, two-dimensional OWC. In [12], authors developed a latching control-based algorithm. This algorithm performs by opening and closing high velocity stop valve of the OWC air turbine.

In [13] and [14], the authors examined control systems such as PI, proportional integral derivative, and fuzzy theory for doubly fed induction generator (DFIG) OWC power plants. However, using closed-loop algorithms, these control solutions reduce flow rate constraints. Based on the analysis of available literature, we can optimize the Wells turbine for the lowest losses by regulating the speed and valve area to achieve a satisfactory flow rate and coefficients. Hence, the proposed stage one aims to improve PTO performance by applying maximum power point tracking (MPPT) technique.

B. Stage Two

The PMSG's analytical model and control are fundamentally complex. It consists of non-linearity and multi-variable characteristics, making it susceptible to parametric changes and disturbances caused by unknown factors [15]. Therefore, it is required to achieve robust performance of the PMSG-based OWEC systems. To accomplish this, various conventional control methods are developed in renewable energy applications [15]–[17]. However, renewable systems often use PI-based solutions, which are widely popular among existing control strategies. Conversely, the PMSG-based OWEC system could be inefficient due to its non-linear nature, in contrast to the PI controller's linear nature. Also, it has been observed through existing demonstrations that non-linear adaptive back-stepping control has enhanced resilience and regulation capability compared to conventionally controlled power systems such as field-oriented control (FOC) and direct torque-power control [18], [19]. As a result, the Lyapunov stability method can reduce the impact of dynamic non-linearities and uncertainty in the second stage of the control solution. It ensures the PMSG-based OWEC system's robustness and provides significant tracking responses with reduced errors, as demonstrated in Section VI. Nevertheless, we can achieve adaptive control by implementing two primary steps. The primary objective of the first step is to eliminate the speed-tracking error, assuming that the relevant aspects of the OWEC system are already known. Hence, in the proposed second stage, we can determine the final stator voltage references.

The researchers investigated various nonlinear control schemes [20]–[22]. In [20], the authors presented a derivation of a robust nonlinear controller to regulate the speed of a PMSG. This derivation considers adaptive control laws. However, in contrast to adaptive control, the sliding mode control (SMC) technique also offers advantages for nonlinear systems. The advantages include high flexibility, a high convergence rate, and ease of implementation [21]. Along with its pros, one of the main problems with SMC is that it can chatter, making it less useful in generation systems prone to high-frequency harmonics [22]. Moreover, the unpredictable nature of the OWEC system reduces the control's efficiency in harvesting robust electrical energy. Therefore, this paper has specifically designed an adaptive back-stepping control strategy. The proposed strategy addresses the parametric irregularities that arises from the PMSG OWEC system. Hence, stage two integration assures robust PMSG control.

C. Stage Three

Environmental uncertainty significantly impacts the availability and reliability of offshore or islanded OWEC systems [23]. In OWEC systems, the significance of this argument becomes more reasonable. WECs may also have problems with their sensors, actuators, and converters because they run long distances.

It leads to a decrease in control effectiveness which potentially results in the failure of an entire generation system [24]. In this context, the system's reliability may decrease in a fault scenario. This particular scenario can also disrupt the functioning of the power system, resulting in financial consequences. Also, the failure rate of power electronic devices exhibits a direct relationship with non-linear dynamics and the unstructured uncertainty of marine systems.

Another major challenge is the need for more confidence in installing and operating equipment to extract energy from tides and waves [25]. The novelty and limited monitoring of WEC devices primarily contribute to a lack of data on their malfunctions. This lack of data makes it difficult to understand how WEC systems and their parts fail, how damage and wear can affect OWEC systems and cause them to fail, and how reliable these devices are. Consequently, it becomes challenging to obtain uninterrupted electricity from an OWEC system. Thus, stage three aims to overcome this challenge by reducing system downtime and improving operational availability. Table I summarizes some of the existing methods based on fault strategies.

Moreover, there has been a recent increase in the nominal power rating of OWEC systems [26]. As a result, power converters must effectively manage high voltage levels and tolerate larger currents. A recent study suggested that using a series-parallel topology with multiple converters could be one way to get around the fact that semiconductor switching devices can only handle a limited amount of power [27]. In this context, the proposed design approach consists of a parallel topology, which can effectively reduce power rating constraints associated with electrical equipment.

Stage three considers an open circuit (OC) fault scenario. For this purpose, we have examined and evaluated the topologies reported in [27]–[29] for fault analysis. The implemented topology has an ability to reduce the filter's overall system cost and size. In this way, the parallel converter topology can provide $K+X$ redundancy, making an adaptively regulated PMSG OWEC system more reliable. Hence, stage three contributes to the long-distance reliability of the OWEC systems.

This paper incorporates a multi-leg FRT system that uses a reconfigurable control unit to ensure that all healthy legs can keep working even if one of the converters stops working. The presented reconfiguration control allows for modifying the post-fault current reference in the inverter side phase legs, allowing them to represent their pre-fault condition precisely. In order to keep system ratings at an appropriate level, the fault-tolerant control (FTC) strategy must operate in degradation mode. However, several reconfiguration control topologies have been documented [29], [30]. In [29], authors reported a technique for recovering a malfunctioning leg, ensuring uninterrupted output. This technique adds auxiliary switches to a redundant leg topology.

TABLE I
SUMMARY OF FAULT-BASED CONTROL STRATEGIES IN OWEC SYSTEMS

Strategies	Advantages/disadvantages	Remarks	Refs.
A non-causal linear optimal control	Maximizing the PTO output while considering parameters of the observer and controller are offline	Undertakes the fault diagnosis in real-time	[5]
Observer-based strategy	Estimating offline parameters	Both actuators and sensors can be subject to fault detection	[32]
Acoustic emission monitoring	Timely diagnosis	Widely employed in analogous systems such as offshore turbines	[33]
Methodology for regulating the damping forces observed in linear generators	The AC-DC/DC-AC converter maintains a stable DC-link voltage without the need for an extra DC chopper circuit or crowbar control	FRT capability integrated with DFIG-based hybrid wind-wave energy system	[34]
Predictive control-based fault analysis	It investigates the reliability of fault-tolerance in AC-DC/DC-AC converters while considering WEC valve correction	Floating OWC OWEC system that can enable continuous operation	[35]
Low voltage ride through controller for GSC	Optimizing power extraction from waves and enhancing FRT capabilities	The dynamic performance is assessed by the implementation of numerical simulations	[36]
Adaptive control and multi-leg fault analysis	Controlled or uncontrolled fixed OWC device and reconfigurable control integration while considering parallel power converters configuration using space vector scheme	Robust FRT capability without shutting down the entire power converter under PM wave spectrum	Proposed OWEC system

D. Stage Four

Integrating renewable sources into the grid creates difficulties due to power fluctuations. These oscillations result in weak electrical power regulations, higher losses, more complicated stability, and lowered ratings for electrical parts, all of which reduce the power efficiency between supply and demand [31]. These inherent limitations challenge achieving maximum performance in grid-connected WECs, necessitating the integration of storage systems. Therefore, the proposed stage four limits power fluctuations in OWC OWEC system. This paper incorporates MPC-EMS to the DC-DC bidirec-

tional converter, improving power quality by smoothing the output power.

It is important to note that PI control is the most commonly utilized control topology among existing EMS options due to its simpler algorithm and superior results. However, designing and selecting parameters for PI controller is challenging. It has slow dynamic reaction, resulting in a delayed stabilization period [37]. Therefore, in conventional methods, minor oscillations remain significant, which decreases charging and discharging efficiency in SCs. Furthermore, the grid connection of OWC power plant is of utmost importance in ensuring power quality. Its Integration may create technical and financial obstacles. In this situation, adopting EMS appears more advantageous because it effectively uses generated ocean wave power as a dispatchable resource within the grid network.

Additionally, the electric grid involves various fundamental system's elements, including production stations, transmission systems, and distribution networks. These systems operate in synchronization to ensure continuous power supply to consumers. Since the power output of WECs fluctuates due to their inherent oscillations. Therefore, power fluctuations have a significant impact on the grid when connected without the appropriate power-smoothing technology. In this particular context, power smoothing entails using appropriate control mechanisms or significant energy storage systems (ESSs).

Previously, researchers have examined the application of ESSs in various renewable energy systems [38], [39]. Although integrating power smoothing technologies involving flywheel and battery systems has attracted considerable recognition, it is worth mentioning that a lack of comprehensive research has been observed regarding the EMS-OWEC systems. However, compared to SCs, batteries achieve their high energy density by allowing them to charge or discharge energy at a slower rate [38]. This characteristic results in a higher overall energy capacity, but a lower power density. As a result, using battery-based EMS solutions is not suited for OWEC systems. Therefore, SC-based power smoothing is an appropriate choice due to its rapid charging and discharging rates, low maintenance criteria, and long lifespan [39].

III. OWC and GSC Control Strategy of the OWEC System

This section presents the modeling of stage one. As shown in Fig. 4, the fixed OWC device comprises two main elements: a partially submerged chamber with an underwater opening at its front and a Wells turbine that links the upper section of the chamber to the atmosphere.

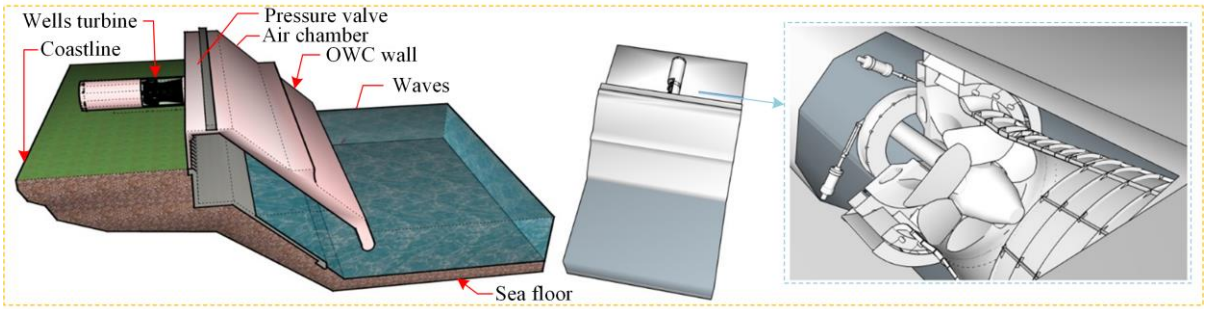

Fig. 4. 3D model of the OWC plant.

A. Wave Energy Spectrum and Wells Turbine Modeling

This paper considers the PM wave energy spectrum. It recommends that under a persistent and consistent airflow over an important geographic expanse, waves will reach a state of equilibrium with the wind. We can illustrate the energy distribution formula as follows [40]:

$$E_{\mathrm{PM}}(\omega_{\mathrm{PM}})=\frac{\alpha g^2}{(\omega_{\mathrm{PM}})^5}\exp\left[-\beta\left(\frac{\omega_{\mathrm{o}}}{\omega_{\mathrm{PM}}}\right)^4\right] \tag{1}$$

where α =8.1×10^{-3}; β =0.74; ω_{PM} is the angular frequency (rad/s); g is the gravity acceleration (m/s^2); and ω_{o} is natural angular frequency (rad/s).

The PM spectrum in the frequency domain can be given as:

$$E_{\mathrm{PM}}(f)=\frac{E_{\mathrm{s}}}{(2\pi)^4 f^5}\exp\left[\frac{-F_{\mathrm{s}}}{(2\pi)^4 f^4}\right] \tag{2}$$

where $E_{\mathrm{s}}=173H_{\mathrm{s}}^2/T_{\mathrm{av}}$ and $F_{\mathrm{s}}=691/T_{\mathrm{av}}^4$; T_{av} is average of peak period of wave records (s); H_{s} represents the significant wave height in meters ($H_{\mathrm{s}}=4\sqrt{S_{\mathrm{w}}\Delta\omega}$); and S_{w} represents the wave energy spectrum.

To identify the real nature of sea waves, we can determine the velocity of airflow as [13]:

$$v_x=\frac{\partial H_{\mathrm{s}}(t)}{\partial t}\left(\frac{A_{\mathrm{O}}}{A_{\mathrm{D}}}\right) \tag{3}$$

where v_x represents the flow velocity (m/s); $H_{\mathrm{s}}(t)$ is the wave amplitude (m); A_{O} shows the chamber cross-sectional area (m^2); and A_{D} is the duct cross-sectional area (m^2).

Dr. Alan Arthur Wells created the Wells turbine at Queen's University in Belfast, United Kingdom, in 1976 [41]. Figure 5 displays the simulink model of the Wells turbine.

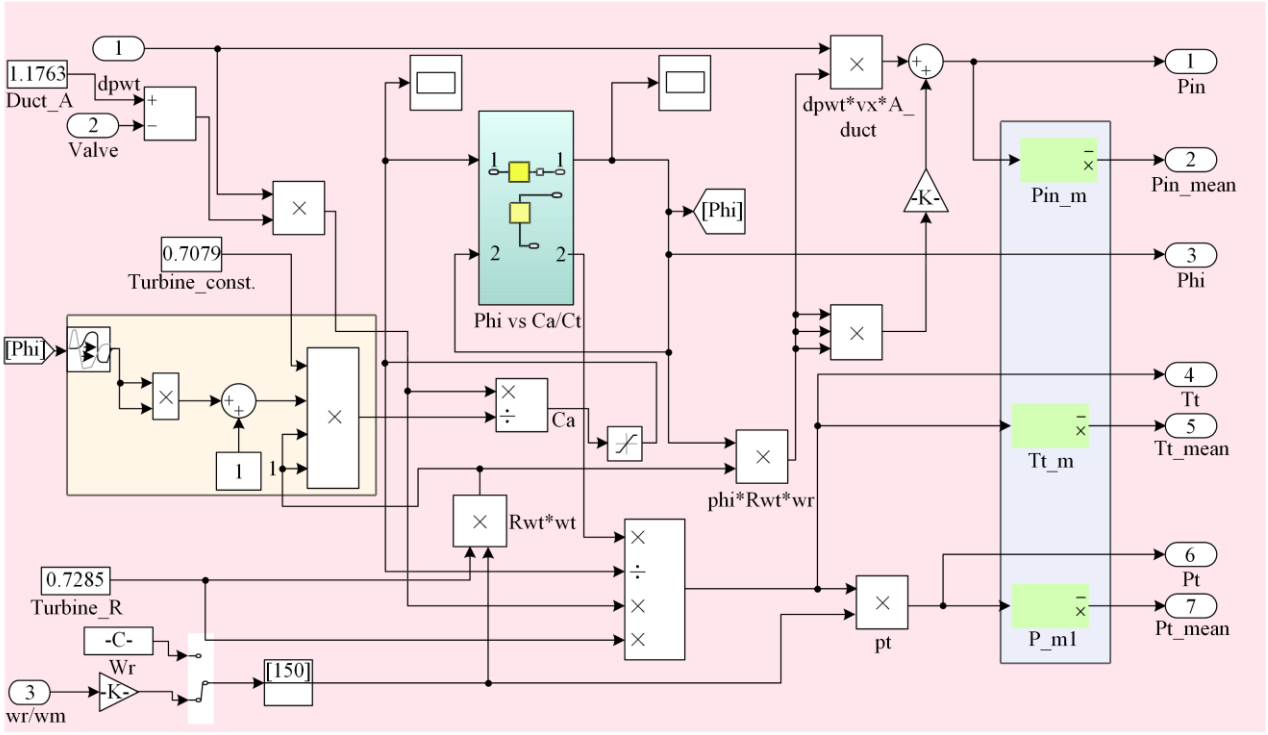

Fig. 5. Matlab/Simulink subsystem of the Wells turbine.

The mathematical modeling of Wells turbines can be formulated as follows [13], [42]:

$$K_{\mathrm{t}} = 0.5\rho_{\mathrm{a}} b_{\mathrm{wt}} n_{\mathrm{wt}} l_{\mathrm{wt}} \tag{4}$$

$$\varphi_{\mathrm{f}} = \frac{v_x}{R_{\mathrm{wt}}\Omega_{\mathrm{r}}} \tag{5}$$

$$\Omega_{\mathrm{r}}^{*} = \omega_{\mathrm{r}}^{*} = \frac{v_{x\_\mathrm{mean}}}{R_{\mathrm{wt}}\varphi_{\max}} \tag{6}$$

$$P_{\mathrm{in}} = A_{\mathrm{D}} v_x (0.5\rho_{\mathrm{a}} v_x^2 + \Delta p_{\mathrm{wt}}) \tag{7}$$

$$\begin{cases} C_{\mathrm{a}} = \dfrac{2A_{\mathrm{D}}\Delta p_{\mathrm{wt}}}{\rho_{\mathrm{a}} b_{\mathrm{wt}} n_{\mathrm{wt}} l_{\mathrm{wt}} \left[v_x^2 + (R_{\mathrm{wt}}\Omega_{\mathrm{r}})^2\right]} \\ C_{\mathrm{t}} = \dfrac{2T_{\mathrm{m}}}{\rho_{\mathrm{a}} b_{\mathrm{wt}} n_{\mathrm{wt}} l_{\mathrm{wt}} R_{\mathrm{wt}} \left[v_x^2 + (R_{\mathrm{wt}}\Omega_{\mathrm{r}})^2\right]} \end{cases} \tag{8}$$

$$\Delta p_{\mathrm{wt}} = \frac{K_{\mathrm{t}} C_{\mathrm{a}} \left[v_x^2 + (R_{\mathrm{wt}}\Omega_{\mathrm{r}})^2\right]}{A_{\mathrm{D}}} \tag{9}$$

$$\begin{cases} T_{\mathrm{m}} = T_{\mathrm{t}} = K_{\mathrm{t}} C_{\mathrm{t}} R_{\mathrm{wt}} \left[v_x^2 + (R_{\mathrm{wt}}\Omega_{\mathrm{r}})^2\right] \\ T_{\mathrm{m}} = A_{\mathrm{D}} R_{\mathrm{wt}} \dfrac{C_{\mathrm{t}}}{C_{\mathrm{a}}} \Delta p_{\mathrm{wt}} \end{cases} \tag{10}$$

$$\begin{cases} \eta_{\mathrm{wt}} = \dfrac{P_{\mathrm{m}}}{P_{\mathrm{in}}} = \dfrac{\Omega_{\mathrm{r}} T_{\mathrm{m}}}{\Delta p_{\mathrm{wt}} Q_{\mathrm{f}}} = \\ \dfrac{\Omega_{\mathrm{r}} K_{\mathrm{t}} C_{\mathrm{t}} R_{\mathrm{wt}} \left[v_x^2 + (R_{\mathrm{wt}}\Omega_{\mathrm{r}})^2\right]}{\dfrac{K_{\mathrm{t}} C_{\mathrm{a}} \left[v_x^2 + (R_{\mathrm{wt}}\Omega_{\mathrm{r}})^2\right]}{A_{\mathrm{D}}} v_x A_{\mathrm{D}}} = \\ \dfrac{\Omega_{\mathrm{r}} R_{\mathrm{wt}} C_{\mathrm{t}}}{C_{\mathrm{a}} v_x} = \dfrac{C_{\mathrm{t}}}{C_{\mathrm{a}} \varphi_{\mathrm{f}}} \end{cases} \tag{11}$$

where K_{t} shows the turbine constant (kg/m); ρ_{a} represents the air density (kg/m^3); b_{wt} gives the blade height (m); n_{wt} donates the turbine blades number; l_{wt} represents the blade chord length (m); φ_{f} shows the flow coefficient of a turbine, R_{wt} is the Wells turbine mean radius (m); Ω_{r} or ω_{r} denotes rotational speed of turbine (rad/s); Ω_{r}^{*} or ω_{r}^{*} are the reference rotational speeds (rad/s); v_{x_mean} is the optimum mean speed (m/s); $\varphi_{\max}$ gives the threshold value for optimal flow; P_{in} denotes the pneumatic or available power inside the chamber (W); C_{t} and C_{a} are the Wells turbine torque and power coefficient, respectively; Δp_{wt} represents the chamber pressure drop (Pa); T_{m} or T_{t} are the Wells turbine torques; P_{m} or P_{t} are Wells turbine powers (W); Q_{f} is the flow rate (m^3/s); and η_{wt} shows the efficiency of the turbine.

The mathematical expression for the average efficiency of the Wells turbine is given as follows [13]:

$$\eta_{\mathrm{avg}} = \frac{\dfrac{1}{T}\displaystyle\int_0^T (\Omega_{\mathrm{r}} T_{\mathrm{m}})\,\mathrm{d}t}{\dfrac{1}{T}\displaystyle\int_0^T (\Delta p_{\mathrm{wt}} Q_{\mathrm{f}})\,\mathrm{d}t} \tag{12}$$

where T represents the time period (s).

The characteristic curves of the C_{t} and C_{a} with respect to the flow coefficient of the Wells turbine can be derived as [42]:

$$\begin{cases} C_{\mathrm{t}} = \dfrac{\sum_{n=0}^{6} p_n \varphi_{\mathrm{f}}^{n-1}}{\sum_{n=0}^{4} q_n \varphi_{\mathrm{f}}^{n-1}} \\ C_{\mathrm{a}} = 4.8\varphi_{\mathrm{f}} + 18.8\varphi_{\mathrm{f}}^{\,2} - 25\varphi_{\mathrm{f}}^{\,3} \end{cases} \tag{13}$$

1) Optimal Power Extraction Scheme of the Wells Turbine

High-pressure oscillations can significantly reduce the efficiency of a Wells turbine-driven OWC device. Two factors contribute to lower Wells turbine efficiency, i.e., the turbine's oscillating airflow and the flow rate increment that surpasses the predetermined threshold of 0.3 [13]. Due to above factors, mechanical efficiency significantly drops, resulting in lower power generation. Therefore, we aim to efficiently apply MPPT by taking into account the optimized power characteristics of the Wells turbine. Consequently, we can express the optimal φ_{f} as:

$$0.26 \leqslant \varphi_{\mathrm{f}} \leqslant 0.3 \tag{14}$$

Two separate kinds of controllers have been considered to achieve optimized control of the OWC chamber valve, i.e., the PI and FOPID controllers. The PI controller is widely recognized as a simple and uncomplicated controller. This controller's effortless structure contributes to its success. However, the proposed FOPID-based solution would be more suitable than the PI controller for extracting power efficiently. A PI controller compares the obtained power to the reference power and then transmits the resulting error to the controller. We can express the Laplace transfer function of a PI controller as follows:

$$V(s) = K_{\mathrm{P}} + \frac{K_{\mathrm{I}}}{s} = \frac{K_{\mathrm{P}} s + K_{\mathrm{I}}}{s} = \frac{K_{\mathrm{P}}(s + K_{\mathrm{I}}/K_{\mathrm{P}})}{s} \tag{15}$$

where K_{P} and K_{I} represents the proportional and integral gains, respectively.

Based on Section VI findings, the FOPID controller offers superior performance in regulating the valve position to limit the Q_{f} compared to the PI controller. Figure 6 illustrates the layout of the FOPID controller. The FOPID controller precisely lowers stalling phenomena by regulating the v_x within the turbine's requirements.

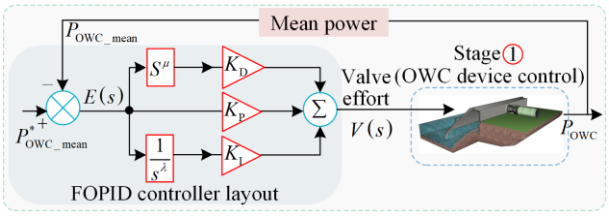

Fig. 6. Proposed OWC control scheme.

Moreover, the control mechanism that has been implemented starts its operation in the presence of an irregular wave spectrum and generates a reference torque that is proportional to the rotor speed. The mean block delivers the OWC power and evaluates it with the intended output power. Finally, the error signal is conveyed to the FOPID-based valve controller and is given as [14]:

$$e(t) = \overline{P^{*}_{\mathrm{OWC}}} - \overline{P_{\mathrm{OWC}}} \tag{16}$$

where the desired mean power is denoted as $\overline{P^{*}_{\mathrm{OWC}}}$; and $\overline{P_{\mathrm{OWC}}}$ represents the mean measured power.

The equations defining the FOPID controller are as follows:

$$\begin{cases} v(t) = K_{\mathrm{I}} S^{-\lambda} e(t) + K_{\mathrm{P}} e(t) + K_{\mathrm{D}} S^{\mu} e(t) \\ \dfrac{V(s)}{E(s)} = K_{\mathrm{P}} \left(T_{\mathrm{D}} s^{\mu} + \dfrac{1}{T_{\mathrm{I}} s^{\lambda}} + 1 \right) \end{cases} \tag{17}$$

where $V(s)$ and $E(s)$ are the Laplace transforms of $v(t)$ and $e(t)$, respectively; λ and μ represents the two non-integer orders; K_{P}, T_{D} and T_{I} are representing the proportional, differential and integral gains, respectively.

To enhance the OWC device optimization, a significant correspondence has been determined between the chamber pressure and the reference speed, which provides a consistent path to maximize power generation. Since Ω_{r} determines the operational performance of the OWC plant and serves as feedback for the controller, therefore, the presence of oscillations can be referred to the selection of PI parameters. The tuned controller and a suitable scaling can restrict these oscillations by implementing a satisfactory torque control scheme. Finally, the obtained speed enhances the performance of the OWC plant at corresponding Ω^{*}_{r}.

2) PMSG Modeling

The PMSG OWEC system is a popular power system due to several benefits, such as its ease of control and high torque-to-inertia ratio. The design of the PMSG dynamic model is formulated by utilizing the voltage and flux equations. We can represent the mathematical formulation of a PMSG in the *dq* reference frame as follows [43]:

$$\begin{cases} v_{ds} = R_{\mathrm{s}} i_{ds} + L_d \dfrac{\mathrm{d}i_{ds}}{\mathrm{d}t} - \omega_{\mathrm{e}} \psi_{qs} \\ v_{qs} = R_{\mathrm{s}} i_{qs} + L_q \dfrac{\mathrm{d}i_{qs}}{\mathrm{d}t} + \omega_{\mathrm{e}} \psi_{ds} \end{cases} \tag{18}$$

where ψ_{ds} and ψ_{qs} are the flux linkages of the *dq* axis, i_{ds} and i_{qs} are the *dq* axis stator currents.

When the *dq* axes rotate at synchronous speed, the *d*-axis becomes aligned with the rotor. Therefore, the stator flux components can be given as follows:

$$\begin{cases} \psi_{ds} = L_d i_{ds} + \psi_{\mathrm{f}} \\ \psi_{qs} = L_q i_{qs} \end{cases} \tag{19}$$

where L_d and L_q are the inductance of the *dq* axis.

By substituting relevant variables into the given equations, the following set of mathematical expressions can be derived:

$$\begin{cases} v_{ds} = R_s i_{ds} + L_d \dfrac{\mathrm{d}i_{ds}}{\mathrm{d}t} - i_{qs} L_q \omega_e \\ \dfrac{\mathrm{d}i_{ds}}{\mathrm{d}t} = \dfrac{1}{L_d}(-R_s i_{ds} + \omega_e i_{qs} L_q + v_{ds}) \end{cases} \tag{20}$$

$$\begin{cases} v_{qs} = R_s i_{qs} + L_q \dfrac{\mathrm{d}i_{qs}}{\mathrm{d}t} + \omega_e \psi_{ds} \\ \dfrac{\mathrm{d}i_{qs}}{\mathrm{d}t} = \dfrac{1}{L_q}(-R_s i_{qs} - \omega_e i_{ds} L_d - \omega_e \psi_f + v_{qs}) \\ \dfrac{\mathrm{d}i_{qs}}{\mathrm{d}t} = \dfrac{1}{L_q}(-R_s i_{qs} - \omega_e \psi_f + v_{qs}) \end{cases} \tag{21}$$

To achieve maximum electromagnetic torque, it is necessary to set the initial value of the i_{ds} to zero. The PMSG torque can expressed as:

$$T_e = 1.5P\left[\psi_f i_{qs} + (L_d - L_q) i_{ds} i_{qs}\right] = 1.5P\psi_f i_{qs} \tag{22}$$

where T_e represents the generator's electromagnetic torque. The implemented system model of the generation side is shown in Fig. 7. The relationship between T_m and T_e can be mathematically represented as:

$$\begin{cases} T_m - T_e = \Omega_r B + J \dfrac{\mathrm{d}\Omega_r}{\mathrm{d}t} \\ \dfrac{\mathrm{d}\Omega_r}{\mathrm{d}t} = \dfrac{T_m - T_e - \omega_e B}{J} \end{cases} \tag{23}$$

$$\frac{\mathrm{d}\theta_e}{\mathrm{d}t} = \omega_e = \Omega_r P \tag{24}$$

where *B* represents the frictional coefficient and *J* shows the inertia.

When i_{ds} =0, the (20) becomes (25), and the active and reactive powers of a PMSG can be expressed as follows:

$$v_{ds} = -\omega_e i_{qs} L_q \tag{25}$$

$$\begin{cases} P_g = 1.5(v_{ds} i_{ds} + v_{qs} i_{qs}) \\ Q_g = 1.5(v_{ds} i_{qs} + v_{qs} i_{ds}) \end{cases} \tag{26}$$

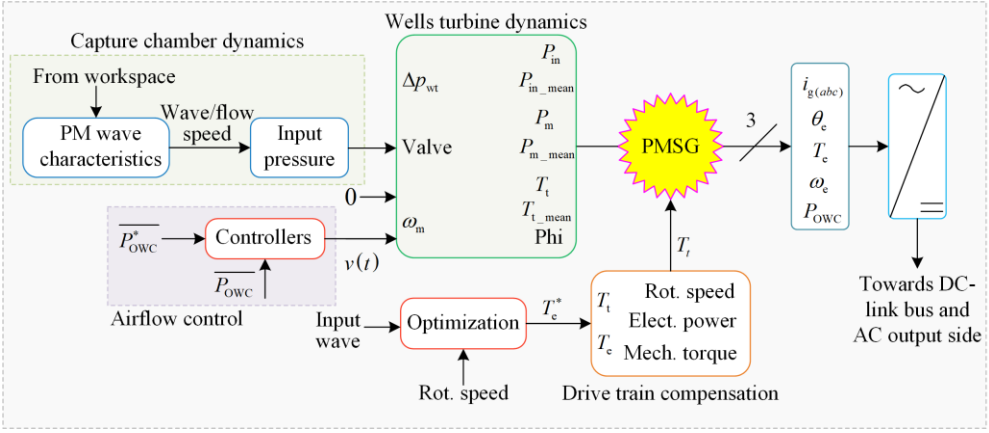

Fig. 7. Illustration of the OWC plant.

B. GSC Control Strategy of the OWEC System

This subsection aims to design stage two of the proposed PMSG OWEC system. We have designed robust controllers that follow the desired trajectory. Based on (18) and (22), it is evident that the model exhibits a significant degree of non-linearity due to the interrelated relationship between electric currents and rotational speed. Hence, the objective is to utilize adaptive control laws that regulates the GSC through reference voltages.

1) Adaptive Back-stepping Control Strategy

Section II comprehensively addressed the effectiveness of the back-stepping design as an adaptive control mechanism for non-linear systems. Therefore, the proposed system's efficiency lies in its ability to deal with non-linear parameters effectively. As shown in Fig. 8, the selected technique utilizes feedback linearity to remove non-linearities efficiently.

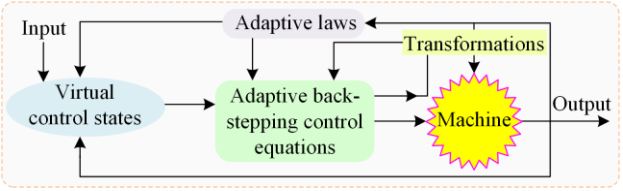

Fig. 8. Framework of the adaptive control design.

Furthermore, permanent magnets generate the magnetic flux in the rotor. It exhibits rotational velocity that is comparable to stator synchronism. This control mechanism regulates the generator's performance by manipulating the mechanical rotational velocity. Also, the control mechanism is based on vector control of the stator voltages. It implies that the reference voltages are necessary to establish control signals for rectifier legs on the generation side.

The control design considers optimal Lyapunov functions, generating a virtual control input that systematically develops the regulation laws. The *dq* transformations can add final gate signals using the space

vector pulse width modulation (SVPWM) method, enabling the necessary GSC control execution. The proposed adaptive back-stepping control involves the execution of critical design steps. Nevertheless, the initial step offers the essential directives for the next step. The control vectors are selected in such a way that $[\boldsymbol{x}]=[x_1 x_2 x_3]^{\mathrm{T}}=[i_{ds} i_{qs} \Omega_{\mathrm{r}}]^{\mathrm{T}}$ as state vectors, and $\boldsymbol{u}=[v_{ds} v_{qs}]^{\mathrm{T}}$ serves as a control vector.

2) Back-stepping Rotational Speed Regulation

To start the procedure of solving irregularities in the speed-tracking step, it is essential to establish the speed tracking error of state variable x_3, which is quantified as a difference between Ω_{r}^* and Ω_{r}.

$$\xi_{\omega}=\Omega_{\mathrm{r}}^*-\Omega_{\mathrm{r}} \tag{27}$$

where Ω_{r}^* and Ω_{r} represents the projected speed trajectory, and observed speed (rad/s), respectively.

Differentiating ξ_{ω} with respect to the time, and its dynamics can be mathematically expressed as:

$$\begin{cases}\dfrac{\mathrm{d}\xi_{\omega}}{\mathrm{d}t}=\dfrac{\mathrm{d}\Omega_{\mathrm{r}}^*}{\mathrm{d}t}-\dfrac{\mathrm{d}\Omega_{\mathrm{r}}}{\mathrm{d}t} \\ \text{i.e.,} \\ \dot{\xi}_{\omega}=\dot{\Omega}_{\mathrm{r}}^*-\dot{\Omega}_{\mathrm{r}}=-\dot{\Omega}_{\mathrm{r}}= \\ \quad \dfrac{1}{J}\left\{\left[\psi_{\mathrm{f}}+\left(L_d-L_q\right)i_{ds}\right]1.5Pi_{qs}+B\Omega_{\mathrm{r}}-T_{\mathrm{m}}\right\}\end{cases} \tag{28}$$

To maintain the PMSG OWEC system stability, a function has been developed to ensure the effective tracking of the desired signal by the PMSG. This function helps minimize the impact of parametric uncertainty. Therefore, we can mathematically express the Lyapunov function and its derivative as follows:

$$V_1=0.5\xi_{\omega}^2 \tag{29}$$

$$\begin{cases}\dfrac{\mathrm{d}V_1}{\mathrm{d}t}=\xi_{\omega}\dfrac{\mathrm{d}\xi_{\omega}}{\mathrm{d}t} \\ \text{i.e.,} \\ \dot{V}_1=\xi_{\omega}\dot{\xi}_{\omega}= \\ \quad \dfrac{1.5P\xi_{\omega}i_{ds}i_{qs}}{J}(L_d-L_q)-\xi_{\omega}{}^2S_{\omega}+ \\ \quad \dfrac{\xi_{\omega}}{J}(1.5Pi_{qs}\psi_{\mathrm{f}}+B\Omega_{\mathrm{r}}-T_{\mathrm{m}}+\xi_{\omega}JS_{\omega})\end{cases} \tag{30}$$

To obtain a predicted error during the process of stabilizing the *q*-axis current error, it is necessary to match the actual speed of the system with the desired speed. Therefore, it is necessary to maintain a negative value for the derivative of $\dot{V}_1$ to ensure stability. Hence, the virtual control inputs may be defined as follows:

$$\begin{cases}i_{ds}^*=0 \\ i_{qs}^*=\dfrac{2}{3P\psi_{\mathrm{f}}}(T_{\mathrm{m}}-\xi_{\omega}JS_{\omega}-\Omega_{\mathrm{r}}B)\end{cases} \tag{31}$$

The Lyapunov function can be obtained as follows:

$$\dot{V}_1=0>-S_{\omega}\xi_{\omega}{}^2 \tag{32}$$

3) Back-stepping Stator Voltages Regulation

The expression of errors in terms of stator current can be formulated as:

$$\begin{cases}\xi_{ds}=i_{ds}^*-i_{ds} \\ \xi_{qs}=i_{qs}^*-i_{qs}\end{cases} \tag{33}$$

By substituting (31) and (33) into the dynamic speed error equation (28), we obtain the revised equations as follows:

$$\begin{cases}\dot{\xi}_{\omega}=\dfrac{1}{J}\left\{1.5P\left[i_{ds}i_{qs}(L_d-L_q)+i_{qs}\psi_{\mathrm{f}}\right]+B\Omega_{\mathrm{r}}-T_{\mathrm{m}}\right\}= \\ \quad \dfrac{1}{J}\left[\begin{array}{l}1.5\psi_{\mathrm{f}}P(i_{qs}^*-\xi_{qs})-1.5P\xi_{ds}i_{qs}(L_d-L_q)+ \\ B\Omega_{\mathrm{r}}-T_{\mathrm{m}}\end{array}\right] \\ \dot{\xi}_{\omega}=\dfrac{1}{J}\left\{\begin{array}{l}1.5P\psi_{\mathrm{f}}\left[\dfrac{2}{3p\psi_{\mathrm{f}}}(T_{\mathrm{m}}-\xi_{\omega}JS_{\omega}-\Omega_{\mathrm{r}}B)\right]- \\ 1.5P\psi_{\mathrm{f}}\xi_{qs}-1.5P\xi_{ds}i_{qs}(L_d-L_q)+B\Omega_{\mathrm{r}}-T_{\mathrm{m}}\end{array}\right\} \\ \dot{\xi}_{\omega}=\dfrac{1}{J}\left\{-1.5P\left[\xi_{ds}i_{qs}(L_d-L_q)+\xi_{qs}\psi_{\mathrm{f}}\right]-\xi_{\omega}JS_{\omega}\right\}\end{cases} \tag{34}$$

The derivative expression for errors can be stated as follows:

$$\dot{\xi}_{ds}=-\dot{i}_{ds}^*-\dot{i}_{ds}=0-\dot{i}_{ds}=-\dot{i}_{ds} \tag{35}$$

$$\dot{\xi}_{ds}=\frac{1}{L_d}(i_{ds}R_{\mathrm{s}}-p\Omega_{\mathrm{r}}i_{qs}L_q-v_{ds}) \tag{36}$$

$$\dot{\xi}_{qs}=\dot{i}_{qs}^*-\dot{i}_{qs} \tag{37}$$

$$\dot{\xi}_{qs}=\frac{2}{3P\psi_{\mathrm{f}}}\left(-\dot{\xi}_{\omega}JS_{\omega}-B\dot{\Omega}_{\mathrm{r}}\right)+\frac{1}{L_q}\left(\Omega_{\mathrm{r}}Pi_{ds}L_d+\Omega_{\mathrm{r}}P\psi_{\mathrm{f}}-v_{qs}+i_{qs}R_{\mathrm{s}}\right) \tag{38}$$

$$\dot{\xi}_{qs}=\frac{1}{L_q}(P\Omega_{\mathrm{r}}i_{ds}L_d+\Omega_{\mathrm{r}}\psi_{\mathrm{f}}P-v_{qs}+i_{qs}R_{\mathrm{s}})+\frac{2}{3P\psi_{\mathrm{f}}}\left\{\begin{array}{l}-\dfrac{B}{J}(T_{\mathrm{m}}-T_{\mathrm{e}}-B\Omega_{\mathrm{r}})- \\ JS_{\omega}\dfrac{1}{J}\left[\begin{array}{l}1.5P\left(i_{ds}i_{qs}(L_d-L_q)+i_{qs}\psi_{\mathrm{f}}\right)+ \\ B\Omega_{\mathrm{r}}-T_{\mathrm{m}}\end{array}\right]\end{array}\right\} \tag{39}$$

$$\dot{\xi}_{qs}=\frac{1}{L_q}(\Omega_{\mathrm{r}}P\psi_{\mathrm{f}}+\Omega_{\mathrm{r}}Pi_{ds}L_d-v_{qs}+i_{qs}R_{\mathrm{s}})+\frac{2}{3PJ\psi_{\mathrm{f}}}(JS_{\omega}-B)\left[\begin{array}{l}-1.5P\left(\begin{array}{l}i_{ds}i_{qs}(L_d-L_q)+ \\ \psi_{\mathrm{f}}i_{qs}\end{array}\right)+ \\ T_{\mathrm{m}}-B\Omega_{\mathrm{r}}\end{array}\right] \tag{40}$$

The schematics representing the adaptive control strategy is shown in Fig. 9.

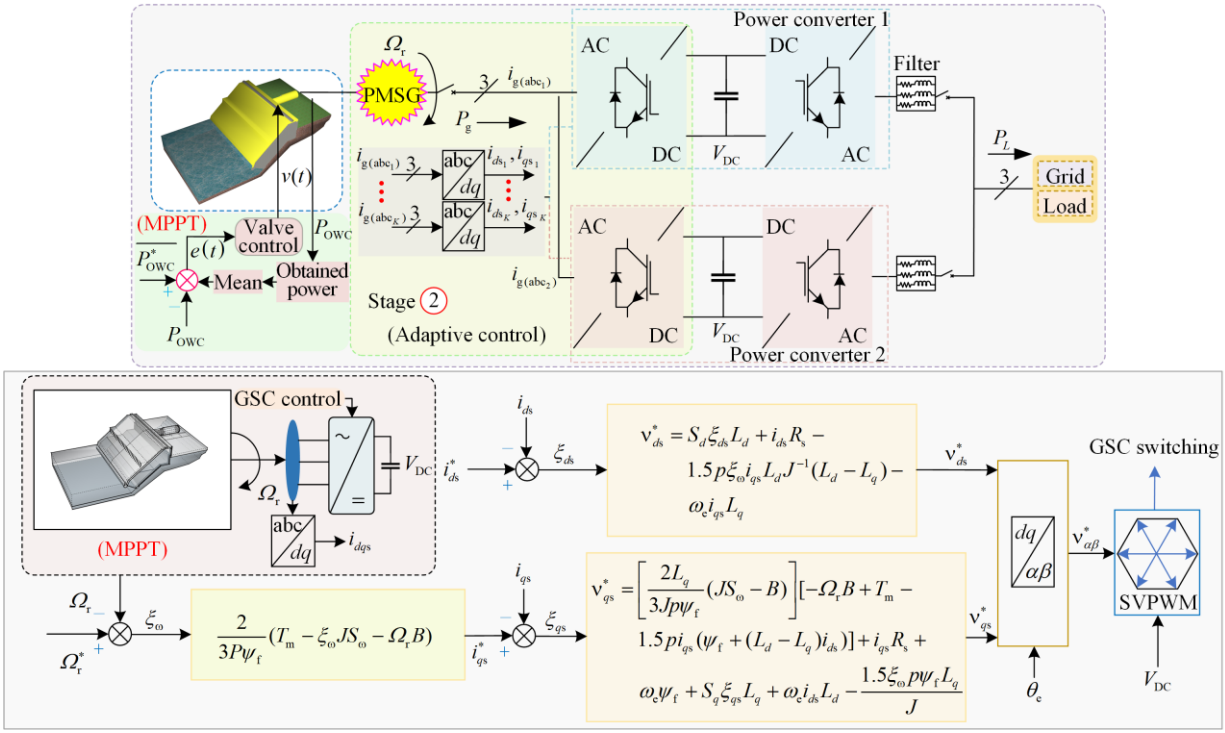

Fig. 9. Schematic representation of the PMSG regulation.

To find the control input for the i_{qs} error trajectory in relation to the final reference voltages, the enhanced Lyapunov function and its derivative are formulated as:

$$V_2 = 0.5\xi_{\omega}^{\ 2} + 0.5\xi_{ds}^{\ 2} + 0.5\xi_{qs}^{\ 2} \tag{41}$$

$$\dot{V}_2 = \xi_{\omega}\dot{\xi}_{\omega} + \xi_{ds}\dot{\xi}_{ds} + \xi_{qs}\dot{\xi}_{qs} \tag{42}$$

$$\begin{aligned}\dot{V}_2 = {} & \frac{1}{J}\xi_{\omega}\left[-1.5p\xi_{ds}i_{qs}(L_d - L_q) - 1.5p\xi_{qs}\psi_{\mathrm{f}}\right] - \\ & S_d\xi_{ds}^{\ 2} - S_q\xi_{qs}^{\ 2} - S_{\omega}\xi_{\omega}^{\ 2} + \\ & \frac{\xi_{ds}}{L_d}(i_{ds}R_{\mathrm{s}} - \omega_{\mathrm{e}}i_{qs}L_q - v_{ds} + \xi_{ds}S_dL_d) + \\ & \frac{\xi_{qs}}{L_q}\left[2L_q\frac{1}{3Jp\psi_{\mathrm{f}}}(JS_{\omega} - B)\begin{pmatrix}-1.5p\psi_{\mathrm{f}}i_{qs} - B\Omega_{\mathrm{r}} - \\ 1.5pi_{ds}i_{qs}\times \\ (L_d - L_q) + T_{\mathrm{m}}\end{pmatrix} + \right. \\ & \left. \omega_{\mathrm{e}}i_{ds}L_d + \omega_{\mathrm{e}}\psi_{\mathrm{f}} + i_{qs}R_{\mathrm{s}} + \xi_{qs}S_qL_q - v_{qs}\right]\end{aligned} \tag{43}$$

To gain the stability of GSC control, it is required that both S_d and S_q exhibit positive numerical values. However, v_{ds} can guarantee the stability of the system. Also, it is necessary to take into account the negative terms present within the Lyapunov derivative function. Hence, the mathematical representation of the reference voltages can be expressed as:

$$v_{ds}^{*} = S_d\xi_{ds}L_d + i_{ds}R_s - 1.5p\xi_{\omega}i_{qs}L_d\frac{1}{J}(L_d - L_q) - \omega_{\mathrm{e}}i_{qs}L_q \tag{44}$$

$$\begin{aligned}v_{qs}^{*} = {} & \frac{2L_q}{3Jp\psi_{\mathrm{f}}}(JS_{\omega} - B)\left[\begin{matrix}-\Omega_{\mathrm{r}}B + T_{\mathrm{m}} - 1.5\times \\ pi_{qs}\left(\psi_{\mathrm{f}} + (L_d - L_q)i_{ds}\right)\end{matrix}\right] + \\ & i_{qs}R_{\mathrm{s}} + \omega_{\mathrm{e}}\psi_{\mathrm{f}} + S_q\xi_{qs}L_q + \omega_{\mathrm{e}}i_{ds}L_d - \frac{1.5\xi_{\omega}p\psi_{\mathrm{f}}L_q}{J}\end{aligned} \tag{45}$$

4) Stator Resistance Regulation

For stator resistance, a Lyapunov function and its derivative can be mathematically expressed as:

$$\begin{cases} V_3 = \dfrac{0.5\Delta R_{\mathrm{s}}^{\ 2}}{z} + 0.5\xi_{\omega}^{\ 2} + 0.5\xi_{ds}^{\ 2} + 0.5\xi_{qs}^{\ 2} \\ \dot{V}_3 = \dot{V}_2 - \Delta R_{\mathrm{s}}\dfrac{\dot{\hat{R}}_{\mathrm{s}}}{z} \\ \dot{\hat{R}}_{\mathrm{s}} = z_1\left(\dfrac{i_{ds}\xi_{ds}}{L_d} + \dfrac{i_{qs}\xi_{qs}}{L_q}\right) \end{cases} \tag{46}$$

where $\Delta R_{\mathrm{s}} = R_{\mathrm{s}} - \hat{R}_{\mathrm{s}}$ and z must have positive values.

The characteristics of the proposed Lyapunov function, including the requisite convergence under estimated parametric uncertainty, exhibits the anticipated stability and can be defined as:

$$\dot{V}_3 = 0 > -S_{\omega}\xi_{\omega}^{\ 2} - S_d\xi_{ds}^{\ 2} - S_q\xi_{qs}^{\ 2} \tag{47}$$

IV. LSC Control Strategy of the OWEC System

This section investigates stage three that consists of parallel converters in an OWC OWEC system. Reliable and sustainable power generation through marine re-

newable sources requires higher protection capabilities. Nevertheless, uncertainties in power semiconductor switch systems result in short or open circuits. Hence, the system could face immediate tripping or damage. In this scenario, we recommend using a parallel converter configuration based on the FTC scheme instead of a single converter [27]. The proposed FTC scheme is illustrated in Fig. 10.

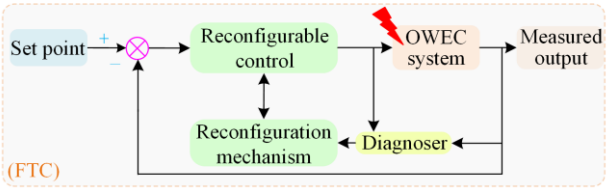

Fig. 10. Reconfigurable control-based FTC scheme.

It is worth noting that an OC fault generally does not result in an immediate power system failure [28]. However, during a fault, the voltages on the inverter side can become distorted. It may contribute to the malfunctioning of the inverters. Therefore, an OC fault analysis is an attempt to simplify the performance evaluation of the OWEC system.

Table II gives the grid-side fault scenarios that may arise in a parallel converter configuration. It shows that the reconfiguration status may vary in certain situations. Therefore, we can potentially define fault cases as:

$$C_{K-x\phi y} \tag{48}$$

where K and x denotes the number of converters and their faulty legs; $\phi=(a,b,c)$ and y are the phases, and its nature, respectively.

The incorporated multi-leg FRT capability performs two types of operations: normal and fault. In the proposed design, switch failures can effectively maintain the normal operation of parallel inverters by utilizing healthy legs. Hence, the parallel converters configuration can effectively manage voltage levels while consistently providing uninterrupted performance. Moreover, it is achievable for the LSC control strategy to precisely track the changed current value when proportional resonant (PR) or hysteresis current controllers are used [44]. The PR controller performs functions within a fixed-coordinate system. Nevertheless, PI controllers can also be used with a non-linear decoupling matrix technique in a rotating synchronous coordinate system. Finally, it generates gate pulses based on SVPWM.

TABLE II
FRT-BASED RECONFIGURATION SCENARIOS

Cases	Fault scenarios		Reconfiguration status
	Power converter 1	Power converter 2	
$C_{1-1\phi y}$	Leg of phase a_1 is faulty	No faulty leg	Yes
$C_{2-2\phi y'}$	Leg of phase a_1 is faulty	Leg of phase b_2 is faulty	Yes
$C_{2-2\phi y}$	Leg of phase a_1 is faulty	Leg of phase a_2 is faulty	No
$C_{2-3\phi y'}$	Leg of phase a_1 and c_1 is faulty	Leg of phase b_2 is faulty	Yes
$C_{2-3\phi y}$	Leg of phase a_1 and c_1 is faulty	Leg of phase a_2 is faulty	No
$C_{2-4\phi y}$	Leg of phase a_1 and c_1 is faulty	Leg of phase a_2 and b_2 is faulty	No

A. Operational and Protection Constraints of an OWEC System

The proposed fault reconfiguration control simplifies the dynamic switching of the parallel power converter switches. It performs the bypassing of faulty legs to maintain regular system operation. However, the following expressions can identify the number of faulty legs, normal legs, post-fault reconfiguration, and relevant rated power relationships as [27]:

$$0 \leqslant l_{F\phi} \leqslant K \tag{49}$$

$$\begin{cases} K = l_{N\phi} + l_{F\phi} \\ l_{N\phi} = K - l_{F\phi} \end{cases} \tag{50}$$

$$\begin{cases} 1 \leqslant (l_{N\phi})^{\min} \\ P_{\text{rated\_}K} = P_K (l_{N\phi})^{\min} \end{cases} \tag{51}$$

where l_{N} and l_{F} represents the normal and faulty leg counts; and P_K denotes the corresponding power.

B. Fault Detection and Isolation Mechanism

To improve the system's reliable performance, fault detection and isolation (FDI) mechanism is adopted in FTC scheme. We have investigated the fault detection technique that was reported in [29], and evaluated its performance under various fault conditions. FDI rectifies the detection error by constantly determining the precise fault position and magnitude. We have taken case 2 from Table II to validate the FRT capabilities. However, the isolation of an OC failure is achieved by removing the corresponding gate signal. In case 2, both converters 1 and 2 exhibit faults in their inverter legs, specifically in phases a_1 and b_2, respectively. Since the remaining legs of both power converters continue to function normally, therefore, we can mathematically represent the voltage estimation of a power converter leg as:

$$v_{\text{lm}} = 0.5V_{\text{DC}}(2I_{\text{l}\phi} - 1) \tag{52}$$

where $I_{\text{l}\phi}$ and V_{DC} represents the switch state and DC-link voltage, respectively.

The fault identification mechanism involves comparing observed voltages with their corresponding predicted values. As indicated in (53), we can achieve the detection of fault occurrence by analyzing the voltage error difference. However, we have implemented voltage and time criteria to prevent inaccurate fault detection. Therefore, the error criteria can be given as follows:

$$\begin{cases} e_{\text{lm}} = v_{\text{lm\_measured}} - v_{\text{lm\_estimated}} \\ e_{\text{lm}} = 0 \rightarrow (\text{ideal}) \\ e_{\text{lm}} > 0 \rightarrow (\text{actual}) \end{cases} \tag{53}$$

Figure 11 depicts a converter in its normal state of operation. The presence of an OC fault is considered in the upper switch. To implement the detection and voltage criterion, the output of the up-counter is integrated into a comparator that includes a variable threshold, denoted as H_c. Also, the time criterion can be utilized to minimize any potential delay in the fault scenario. These delays can be attributed to the overall control system, including the associated switching delays. Hence, a time threshold is applied to minimize the occurrence of inaccurate fault detection. It has an ability to speed up the detection.

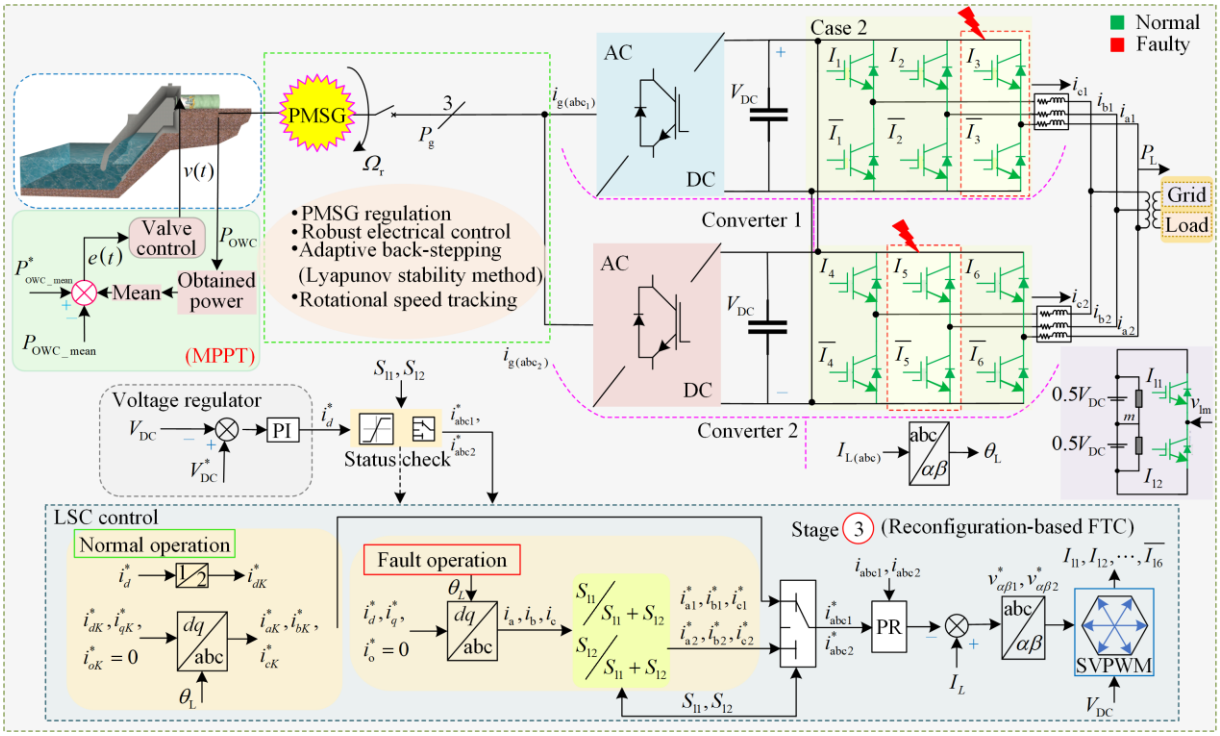

Fig. 11. Schematic representation of the FTC-based OWC OWEC system.

Figure 12 displays the algorithm for the fault status check. The direction of the current also affects overcurrent fault detection time. When the value of $i_1 < 0$, the current flows via the I_1, enabling fault detection. Therefore, we can formalize the expression as follows:

$$T_{\text{L}} = H_{\text{c}} T_{\text{s}} \tag{54}$$

where T_{L} and T_{s} exhibit the threshold and sampling times, respectively.

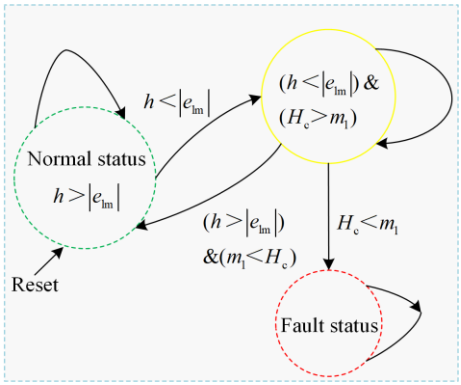

Fig. 12. State flow diagram of fault diagnosis.

C. Reconfiguration and FTC Execution

As shown in Fig. 11, to execute the fault reconfiguration control unit, it is necessary to tune the reference current of the inverter legs based on operational status. A three-phase stationary frame effectively addresses the control of phase currents in the legs. Equation (55) demonstrates that the control design is capable of adapting to both typical and challenging operational scenarios. Also, voltage regulation is achieved by utilizing PI controllers to generate the average value of the i_d^*; after that, this signal is converted into reference outputs through a three-phase stationary frame.

$$S_{\text{lK}} = \begin{cases} 0 \rightarrow \text{fault} \\ 1 \rightarrow \text{normal} \end{cases} \tag{55}$$

The reconfigurable control strategy successfully achieves relevant reference gate signals for LSC control using SVPWM. Furthermore, a status check of the normal leg in *K* converters produces the corresponding reference current. Additionally, implementing a PI controller can successfully address the circulating current problem within power converters legs. Therefore,

we can express their associated current relationships as follows:

$$i_{d\_\lim}^{*}=\begin{cases}K[\max(I)]\rightarrow \text{normal}\\ \min(m_{\mathrm{N}\phi})\rightarrow \text{fault}\end{cases} \tag{56}$$

$$i_{\phi j}^{*}=i_{\phi}^{*}\frac{S_{\phi j}}{\sum_{j=1}^{K}S_{\phi j}} \tag{57}$$

V. Proposed Electrical EMS Control Strategy for the OWEC System

In stage four, to reduce system's complexity, a six-leg power converter is taken into account. In the proposed SC-EMS, it produces voltages on both the generator and grid sides. An MPC-based DC-DC bidirectional converter receives these voltages. The DC-DC bidirectional converter functions as a buck-boost converter and can adjust the EMS voltage in response to variations in the V_{DC} [45].

The DC-DC bidirectional converter comprises of two interconnected control loops and a pair of IGBT switches. However, to obtain the reference SC current for the inner loop, the outer control loop compares the measured V_{DC} with the required V_{DC}^{*}. Therefore, the state of charge (SOC), which depends on the ratio, is a key component of the proposed method. Furthermore, we will determine the energy requirements of the EMS by formulating the time integral of the generated power minus the desired output power. Thus, we can present the expressions as follows:

$$\begin{cases}\lambda=\dfrac{V_{\mathrm{SC}}}{V_{\mathrm{SC\_rated}}}\\ P_{\mathrm{SC}}(t)=P_{\mathrm{OWC}}(t)-P_{\mathrm{L}}(t)\\ E_{\mathrm{EMS}}(t)-E_{\mathrm{EMS}}(t=0)=\int_{0}^{t}P_{\mathrm{SC}}(t)\end{cases} \tag{58}$$

where V_{SC} and $V_{\mathrm{SC\_rated}}$ are the measured and rated SC voltages (V); P_{SC} is SC power (W); P_{OWC} and P_{L} gives the OWC and grid side power (W), respectively.

A SC's appropriate size depends on accurately estimating the necessary energy storage capacity. We can represent the relevant expressions [46] as (59).

As shown in Fig. 13, the MPC-EMS system is considering the cost functions connected to any potential predictions, and the optimization block has the reference value for both buck and boost topologies. However, we can declare the predetermined cost functions [47] as (60).

$$\begin{cases}E_{\mathrm{sc}}=\dfrac{1}{2}C_{\mathrm{SC}}V_{\mathrm{SC}}^{2}\\ C_{eq}=\dfrac{I}{V_{\mathrm{range}}}t\\ C_{\mathrm{SC}}=\dfrac{C_{eq}}{N_{\mathrm{s}}}\\ N_{\mathrm{p}}=\dfrac{I}{I_{\mathrm{SC}}}\\ N_{\mathrm{s}}=\dfrac{V_{\mathrm{range}}}{V_{\mathrm{SC}}}\\ I_{\mathrm{SC}}=C_{\mathrm{SC}}\dfrac{\mathrm{d}V_{\mathrm{SC}}}{\mathrm{d}t}\end{cases} \tag{59}$$

where E_{SC} is the energy storage (Wh); C_{SC} is the SC capacity (F); C_{eq} denotes equivalent capacitance (F); I shows the current through SC (A); V_{range} is the operating voltage range (V); N_{s} and N_{p} shows the number of SCs in series and parallel combination, respectively; and I_{SC} represents the SC current (A).

$$\begin{cases}x_{\mathrm{pre}\_i}(t_{k+1})=f_{\mathrm{pre}}\left\{x(t_k),S_i\right\}\\ g_i=f_g\left\{x^{*}(t_{k+1}),x_{\mathrm{pre}\_i}(t_{k+1})\right\}\\ i=1,2,3,\cdots,n\end{cases} \tag{60}$$

where x_{pre_i} and g_i represents the predicted values, respectively.

The DC-DC bidirectional converter's primary function is keeping the V_{DC}, within the desired rated range. The proposed bidirectional converter enters boost mode when the voltage V_{DC} drops below the lower threshold. After that, it drains the power from the SC and injects it into the DC bus, ensuring that V_{DC} stays below the limit.

Nevertheless, the DC-DC bidirectional converter enters buck mode if the V_{DC} exceeds the upper threshold. It charges the SC while keeping V_{DC} under the upper limit by drawing power from the DC bus. Furthermore, once V_{DC} is within the allowed range, the converter enters idle mode and disconnects the SC from the DC bus.

As shown in Fig. 13, we implemented a low-pass filter to reduce voltage ripples during buck and boost modes. When we assumed the reference signal to be a DC input, it can be represented as (61).

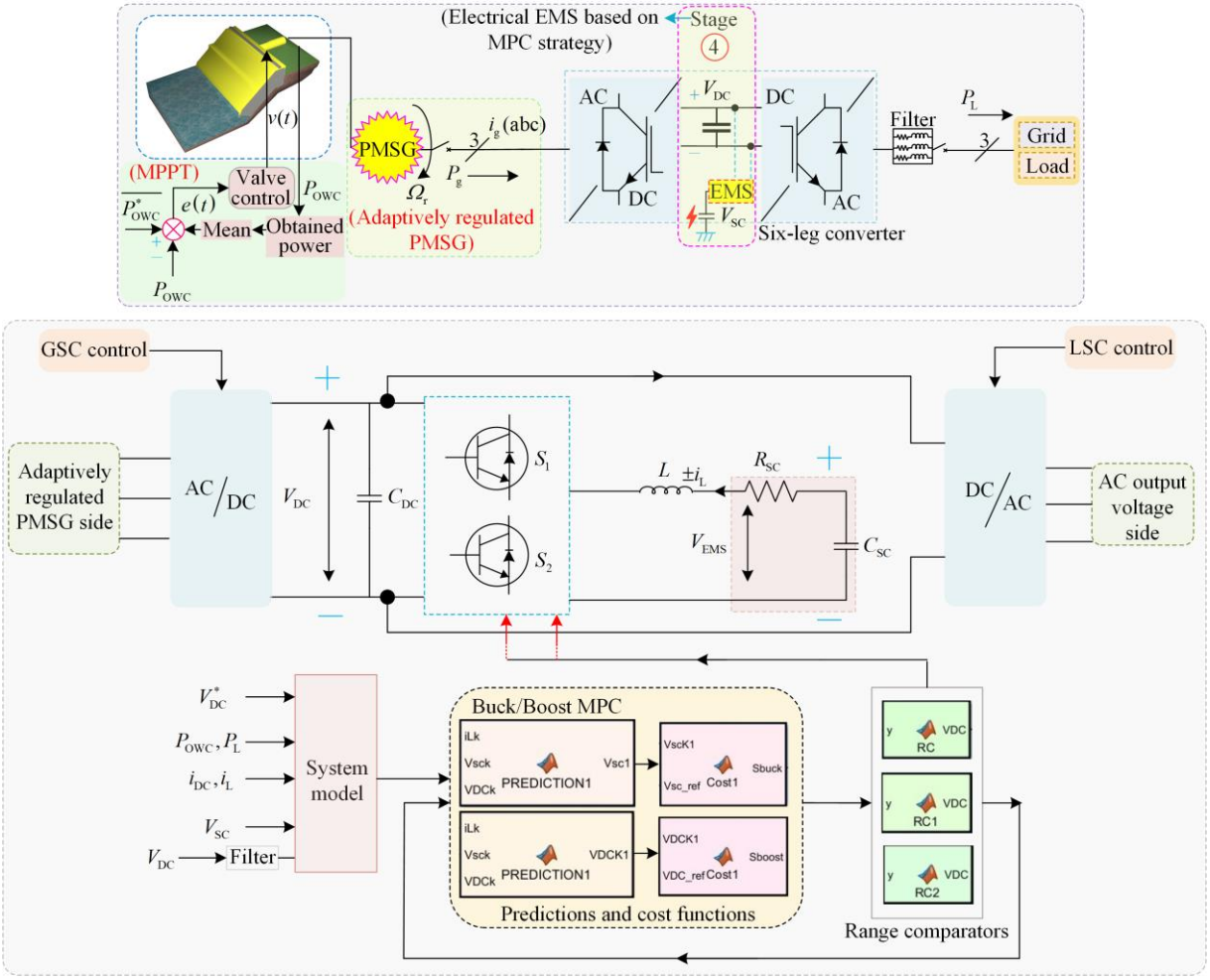

Fig. 13. Schematics of the OWC power smoothing scheme.

$$x^*(t_{k+1}) \approx x^*(t_k) \tag{61}$$

The cost function associated with the buck and boost operation can be defined as:

$$J_{\text{Buck}} = \begin{cases} S_1 = 0, & \left|V^*_{\text{SC}}(k+1) - V_{\text{SC},S_1=0}(k+1)\right| \\ S_1 = 1, & \left|V^*_{\text{SC}}(k+1) - V_{\text{SC},S_1=1}(k+1)\right| \end{cases} \tag{62}$$

$$J_{\text{Boost}} = \begin{cases} S_2 = 0, & \left|V^*_{\text{DC}}(k+1) - V_{\text{DC},S_2=0}(k+1)\right| \\ S_2 = 1, & \left|V^*_{\text{DC}}(k+1) - V_{\text{DC},S_2=1}(k+1)\right| \end{cases} \tag{63}$$

The DC-DC bidirectional converter control executes MPC operational modes, as shown in Fig 14.

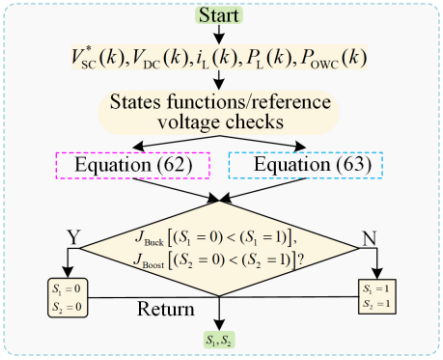

Fig. 14. Algorithm of the bidirectional converter.

The prediction state incorporates the imported variables $V_{\text{DC}}(k)$, $i_{\text{L}}(k)$ and $V_{\text{SC}}(k)$ for the buck-boost operation. It is delivered for optimization from the prediction state $V_{\text{DC}}(k+1)$ while holding predictive values at intervals $t_{k+1} = t_k + T_s$.

After being filtered by a low pass filter, the range comparators determine the triggering of the corresponding operational mode. Hence, the reference terms can be formally stated as follows:

$$\begin{cases} V^*_{\text{SC}}(k+1) \approx V^*_{\text{SC}}(k) \\ V^*_{\text{SC}}(k) = \dfrac{V^*_{\text{Buck}} i_{\text{DC}}(k)}{i_{\text{L}}(k)} \\ V^*_{\text{DC}}(k) = V^*_{\text{DC}}(k+1) \end{cases} \tag{64}$$

where V^*_{DC} and V^*_{Buck} represents the predefined voltages.

VI. Results and Discussions

This section evaluates the MATLAB/Simulink results of the proposed multi-stage design approach for an PMSG OWEC system. Table III provides details re-

garding the system parameters and operating scenarios. To determine generation side performance, we assessed the Wells turbine's power and torque coefficients of the OWC plant. Figures 15(a) and (b), respectively, display Wells turbine coefficients.

TABLE III
SYSTEM OPERATING PARAMETERS

	Parameters	Value
PMSG	Power rating (kW)	60
	Pole pairs	6
	Rotor flux linkage (Wb)	0.58
	Stator winding resistance (Ω)	0.538
	d-axis inductance (H)	$12.98e^{-3}$
	q-axis inductance (H)	$12.98e^{-3}$
	Inertia (kgm^2)	0.55
Wells turbine-based WEC	Pressure drop (kPa)	2.5–8
	Optimal flow coefficient	0.3
	Air density (kg/m^3)	1.225
	Blade length and width (m×m)	0.35×0.23
	Duct area (m^2)	1.17
	Chamber area (m^2)	7.5
	Turbine radius (m)	0.4
	No. of blades	5–8
	Turbine constant	0.7
	Flow rate (m^3/s)	50–150
DC-link and reconfiguration	DC voltage (V)	600
	Voltage threshold	10
	Sampling frequency (kHz)	9–10
Energy storage	SC-EMS rating (kW)	60
	DC terminal voltage (V)	550–650
	Rated capacitance (F)	10
Electrical grid	Voltages (V)	400
	Frequency (Hz)	50

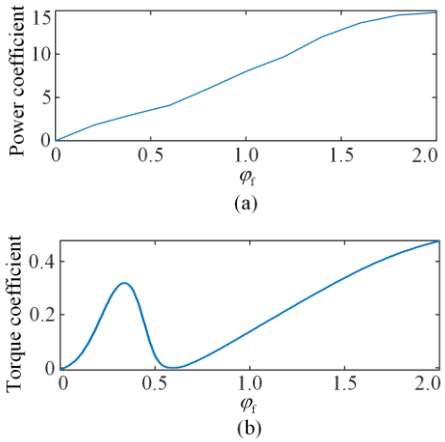

Fig. 15. The Wells turbine characteristics. (a) Power vs. flow coefficient. (b) Torque vs. flow coefficient.

We thoroughly investigated both uncontrolled and controlled OWC WECs, utilizing the four stages of the proposed multi-stage system. We considered an irregular waveform based on the PM spectrum to investigate the realistic effect of ocean waves on the entire OWEC system. Figures 16 and 17, respectively, depicts ocean current's waveform. As depicted in Fig. 17, the OWC chamber exhibits an alternating peak pressure drop of 7.5 kPa.

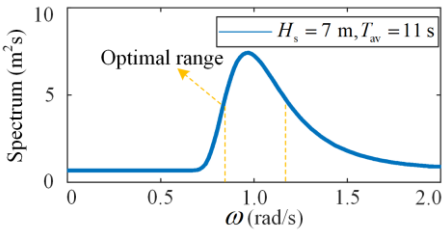

Fig. 16. The PM spectrum for irregular wave strike.

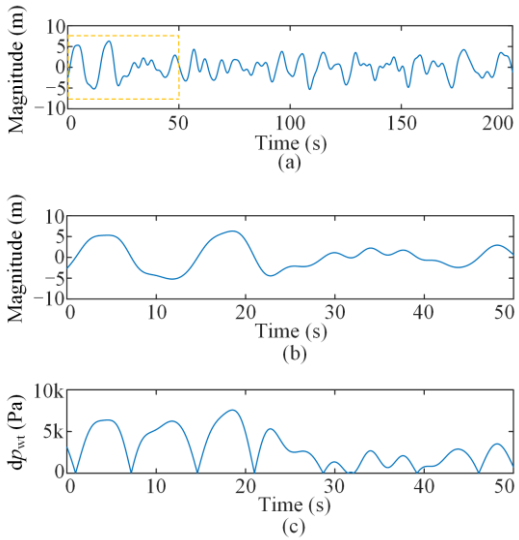

Fig. 17. Irregular waves based on PM spectrum. (a) Wave magnitude. (b) Wave magnitude under 50 s. (c) Chamber pressure drop, Δp_{wt} .

According to (14), the Wells turbine stalls when the φ_f exceeds 0.3. Therefore, it is essential to regulate stalling behavior to achieve optimal performance. Within this particular context, the results show that it offers a satisfactory level of performance while eliminating stalling, enabling the attainment of the desired maximum power output.

Figure 18 illustrates comparison-based findings on the OWC plant performance. We manually select the controller parameters by repeatedly simulating the OWC model, which allows us to analyze various gain values at optimal flow speed. Figures 18 and 19 displays the generated φ_f and Q_f , respectively. An uncontrolled OWC device is inefficient at controlling the Q_f to an appropriate level. Thus, it has a greater tendency to delay and stall. Figure 19 illustrates that airflow control is based on irregular wave input with the implementation of PI and FOPID controllers. Tuning an OWC plant based on PI requires a higher level of accuracy than a FOPID controller. On the other hand, a FOPID controller is performs better at avoiding stalling behavior than a conventional controller.

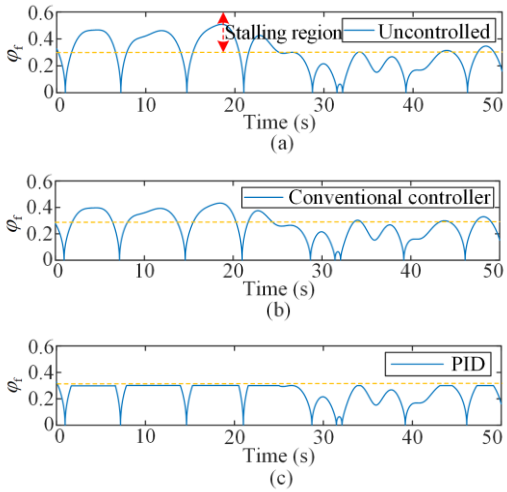

Fig. 18. OWC plant φ_f behaviour. (a) Uncontrolled turbine φ_f. (b) φ_f of conventionally controlled turbine. (c) φ_f based on optimal controller.

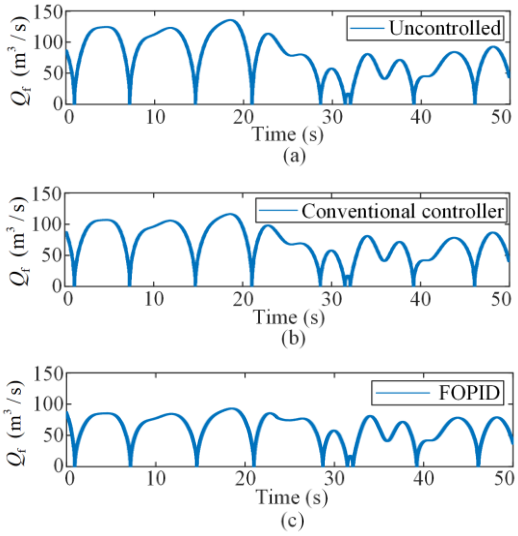

Fig. 19. OWC plant Q_f performance. (a) Q_f of an uncontrolled turbine. (b) Q_f obtained from conventional controller. (c) Fractional order-based Q_f.

Figure 20 shows the Wells turbine's torque in response to flow input. For an uncontrolled OWC device, the turbine torque exceeds 200 Nm. A well-designed and regulated system can effectively control the stalling and robustness of the OWC device. As a result, FOPID OWC plant control effectively prevents stalling occurrences.

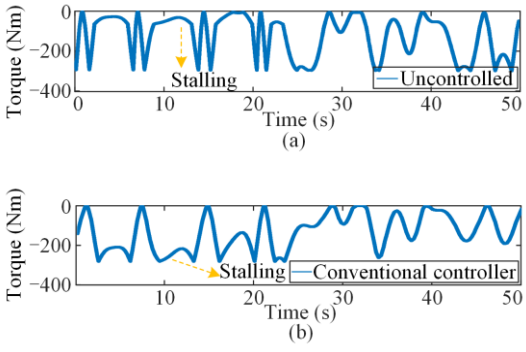

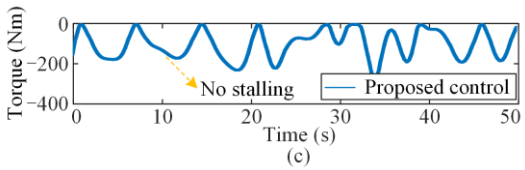

Fig. 20. OWC plant torques. (a) An uncontrolled plant torque. (b). Conventional controller-based plant torque. (c) Controlled OWC plant-based torque.

Moreover, the variations in mechanical speed depend on the performance of the Wells turbine and the speed of the ocean waves. The torque, phase currents, and power generated all appear to be the same as the rotational speed. Hence, the OWEC system produces irregular rotational speed and fluctuating three-phase currents under adaptive control, as observed in Figs. 21 and 22, respectively. From Figs. 21(a) and (b), it can be verified that the rotational speed of the uncontrolled OWC device does not regularly reflect significant oscillations. However, implementing the entire MPPT method requires precise control of the rotational speeds and optimum control of the OWC plant in conjunction with the generator.

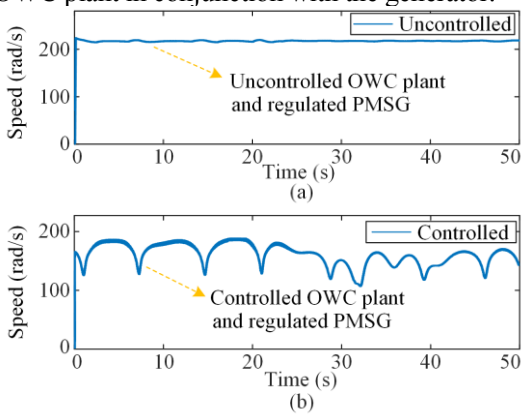

Fig. 21. OWC plant rotational speed performance. (a) Uncontrolled plant. (b) Controlled plant.

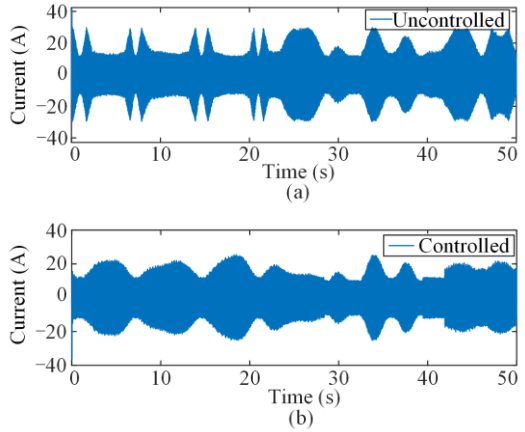

Fig. 22. Generated currents. (a) Current of an uncontrolled plant. (b) Current of controlled plant.

Figure 23 depicts the generated power outputs that is resulted from the implementation of non-linear control. Figure 24 shows that during normal operation, the stage one and two control techniques accurately track the rotational speed reference. The back-stepping control stage and stage one collaborates, allowing the turbine

generator shaft to achieve optimal rotational speed. The PMSG OWEC system robust electrical control effectively responds to chamber Δp_{wt} oscillations.

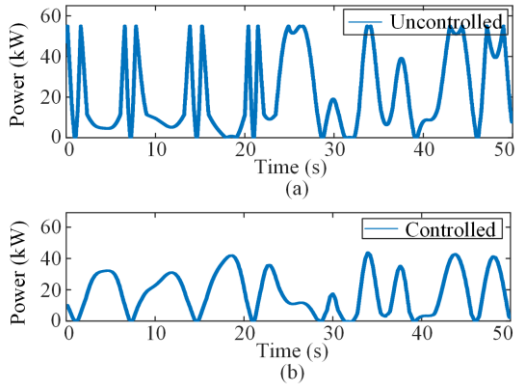

Fig. 23. OWC plant power outputs. (a) Power of an uncontrolled plant. (b) Power of a controlled plant.

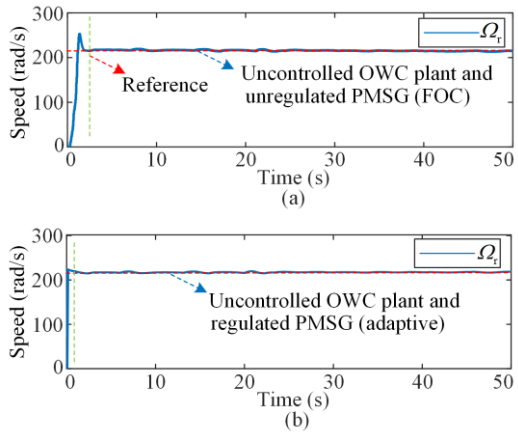

Fig. 24. Electrical control of a PMSG OWEC system. (a) Rotational speed of an uncontrolled system. (b) Rotational speed of a controlled system.

The adaptively regulated PMSG OWEC system, as shown in Fig. 24(b), performs faster than an uncontrolled OWC and an unregulated OWEC system, shown in Fig. 24(a). The proposed approach begins tracking the reference speed within nearly 2 seconds using the Lyapunov stability method, resulting in minimal delay and reduced overshoot. Figure 25 shows the regulated PMSG rotational speed under a controlled OWC device. The controlled OWC and regulated PMSG OWEC systems clearly demonstrate their ability to respond robustly to speed changes. Thus, the proposed non-linear back-stepping control outperforms a traditional control approach, i.e., FOC, in terms of performance.

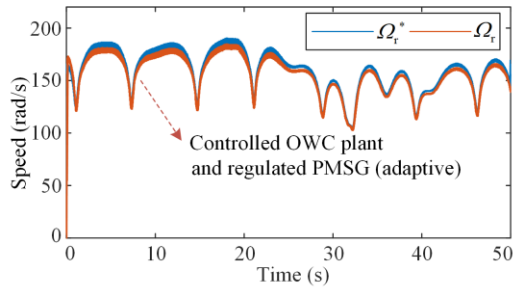

Fig. 25. Rotational speed tracking response of the controlled system.

Furthermore, the implemented adaptive control technique demonstrates insignificant speed and torque errors percentages, shown in Figs. 26(a) and (b), respectively. The Matlab/Simulink tool is considered to evaluate how reliable an adaptively regulated OWEC system is when it comes to FRT capabilities based on fault reconfigurable control. The fault reconfiguration control strategy shows that the inverter legs, i_{a1} and i_{b2}, encountered a fault. If the current is positive, it is not possible to immediately identify the fault. As a result, the positive values of the time conditions are insufficient for identification. However, when the negative current develops and approaches the desired counter-threshold value, we recognize the fault at $t = 31.7983$ s. Thus, based on the detection of the faults, the control initiates operation at $t = 31.811$ s.

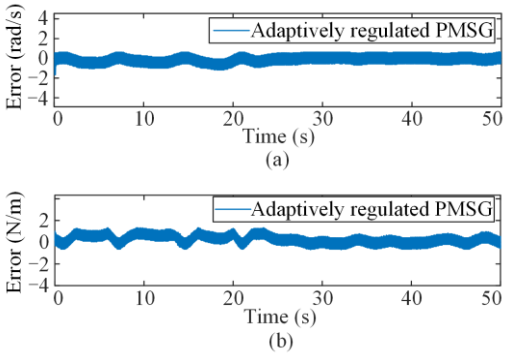

Fig. 26. Adaptive control strategy-based errors. (a) Rotational speed error. (b) Generated torque error.

Figures 27 and 28, shows the generated scenarios, respectively. Because of a failure in power converters 1 and 2, they do not fully withdraw from the system. Power converter 2 reconfiguration initiates during fault operation after the fault detection counter hits the predefined threshold value, $N = 30$. In Figs. 27(b) and 28(c), the FRT capability-based parallel converter of the adaptively controlled PMSG OWEC system starts to reconfigure after a fault at $t = 31.825$ s, respectively. As a result, to compensate for the malfunctioning leg of converter 2, the pre-fault current of converter 1 increases beyond its normal rating while keeping the remaining normal legs active.

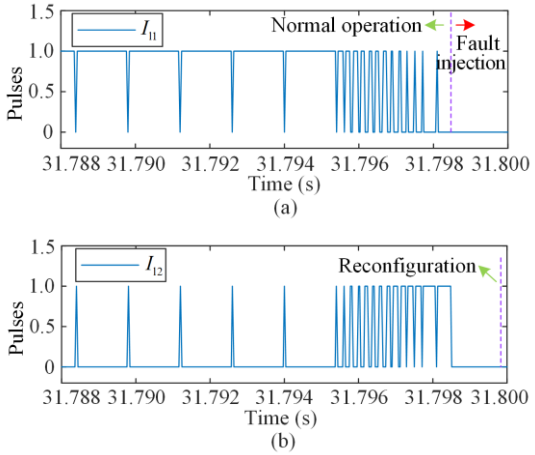

Fig. 27. Gate pulses of inverter legs. (a) Normal and fault operation. (b) Reconfiguration operation.

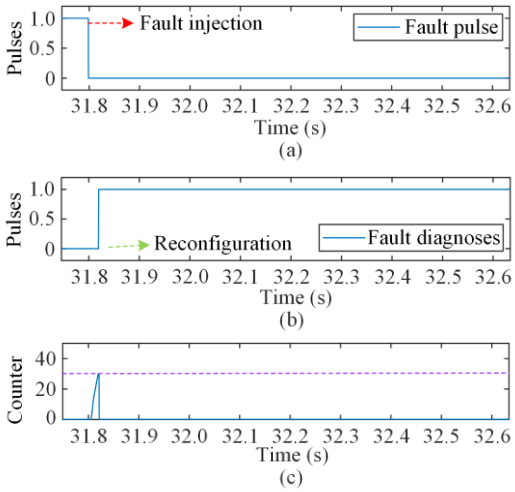

Fig. 28. FRT capability of the OWC OWEC system. (a) Fault detection. (b) Reconfigurable control pulse. (c) Counter for triggering reconfiguration operation.

Figure 29 shows the three-phase currents behavior on the inverter side of an OWC OWEC system. It is worth noting that the reconfigurable control system exhibits rapid dynamic behavior due to its efficient fault detection capabilities. Therefore, by removing the faulty legs and fully utilizing all the healthy ones, the proposed third stage achieves sustainability. As a result, the integrated reconfigurable control makes parallel ocean wave power converters easier to implement and offers multiple-leg FRT capability. Thus, it ensures reliability for the OWEC system.

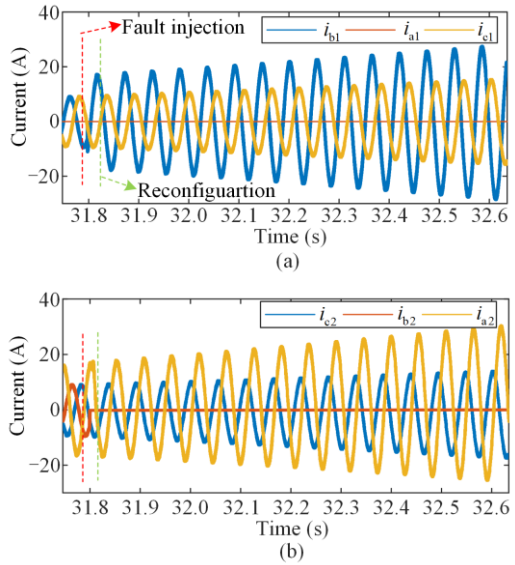

Fig. 29. Parallel converters currents behaviour. (a) Power converter 1. (b) Power converter 2.

Moreover, by implementing SVPWM, the system establishes switching states that lower the inverter's switching frequency. It allows the OWEC system to perform effectively in both normal and fault operations. Therefore, employing SVPWM technique offers more accurate sequence, leading to improved control over the gate signal of a three-phase inverter. From Figs. 27−29, it can be concluded that the FTC scheme improves availibity of parallel converters, and ensures that the OWEC system using an adaptively controlled PMSG is reliable.

The six-leg converter's operation determines the typical V_{DC} link of the OWEC system, as shown in Fig. 30. In stage four, the implementation of MPC DC-DC bi-directional converter prevents irregular wave-based oscillations in both the controlled and uncontrolled OWEC systems. In this separate case, the MPC is responsible for charging and draining the SCs. Figures 31(a) and (b), shows the SC EMS based voltage and current, respectively.

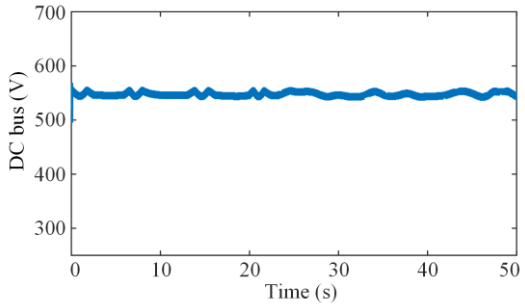

Fig. 30. V_{DC} of an uncontrolled OWC plant.

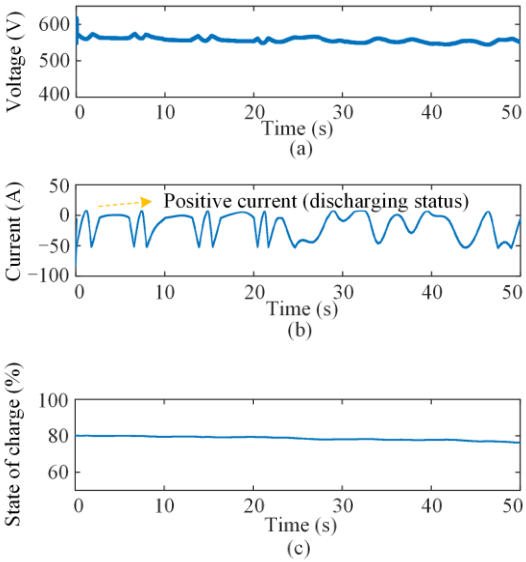

Fig. 31. EMS OWEC system. (a) SC voltage. (b) SC current. (c) SC-SOC.

To configure a SC bank, series connections can made by utilizing capacitors. Figure 31(c) shows the DC-DC bidirectional converter's charge status. If the generated power is less than the grid power, the V_{DC} is controlled by draining the energy storage below its required voltage. In contrast, if the power generated exceeds the power from the grid, charging the EMS maintains the V_{DC} at a nearly stable level.

Furthermore, Fig. 32 demonstrates that incorporating an EMS enables smooth and efficient power transfer

during both bucks and boost operational modes. It is also noticeable that the uncontrolled OWC device generates less power than the controlled device. The Matlab/Simulink results have proven that integrating stage one also leads to a power enhancement of over 28 percent. Hence, stage four achieves the desired fundamental aspect i.e., the power smoothing of an OWC OWEC system.

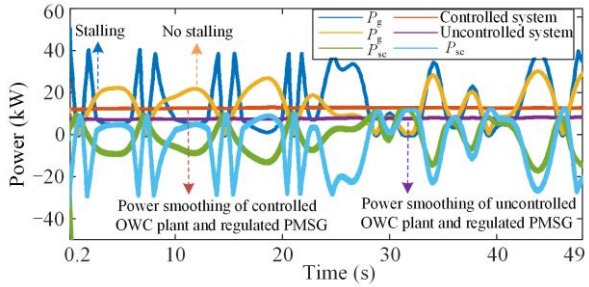

Fig. 32. Power smoothing of OWC OWEC system.

The proposed multi-stage control design approach establishes the WEC's efficient and sustainable performance by optimizing major aspects of the OWEC system. However, we recommend conducting experimental investigations based on control strategies that require integration with actual scenarios to enhance the effectiveness of the OWEC system.

VII. Conclusions

This work presented a new design approach to integrate control strategies for an OWC OWEC system using the Matlab/Simulink tool. The Wells turbine-based WEC responds well to irregular ocean waves generated by the PM wave spectrum. The key findings of the proposed design approach are as follows:

1) Stage one provides a comparative evaluation of the power extraction schemes based on traditional and FOPID controllers. We have verified that these control schemes, through FOPID, outperform traditional ones in controlling the valves of the Wells turbine-based WEC. It eliminates stalling phenomena and improves the fixed OWC device's maximum power-generating abilities.

2) In the second stage, the performance of the PMSG OWEC system was improved using a non-linear adaptive control strategy based on the Lyapunov stability technique. Compared to FOC, the results show that using SVPWM and a non-linear back-stepping control design leads to accurate and robust speed tracking while reducing the percentage of errors.

3) In stage three, incorporating the FRT capability into an OWC OWEC system aims to provide an uninterrupted and reliable power supply. During fault operations, the system can manage the reconfiguration of parallel power converters. Instead of turning off the whole converter, the reconfigurable control unit attempts to use all of the healthy legs by isolating the faulty one.

4) In stage four, a proposed solution for the EMS involves an MPC strategy. A DC-DC bidirectional converter integrates SCs into the six-leg converter DC link. Its incorporation ensured smooth and stable output power.

Finally, the proposed multi-stage control design can improve the global performance of the grid-connected OWC OWEC system, achieving its main objectives of efficiency, robustness, reliability, and power smoothness.

Acknowledgment

Not applicable.

Authors' Contributions

Muhammad Noman: methodology, software, investigation, writing-original draft, visualization. Guojie Li: supervision. Muhammad Waseem Khan: writing-review & editing, formal analysis. Keyou Wang: formal analysis. Bei Han: formal analysis. All authors read and approved the final manuscript.

Funding

This work is supported by the National Natural Science Foundation of China (No. 52107113 and No. 51877133).

Availability of Data and Materials

Not applicable.

Declarations

Competing interests: The authors declare that they have no known competing financial interests or personal relationships that could have appeared to influence the work reported in this article.

Authors' Information

Muhammad Noman received the B.Sc. degree in electrical engineering from the University of Lahore, Pakistan in 2014, and the M.Sc. in electrical engineering from Southeast University, Nanjing, China, in 2018. He is currently pursuing a Ph.D. degree in electrical engineering at Shanghai Jiao Tong University, Shanghai, China. His research interests include renewable energy, power converters, and hybrid power Systems.

Guojie Li received the B.Eng. and M.E. degrees in electrical engineering from Tsinghua University, Beijing, China, in 1989 and 1993, respectively, and the Ph.D. degree in electrical engineering from Nanyang Technological University, Singapore, in 1999. He was an associate professor with the Department of Electrical Engineering, Tsinghua University. He is currently a

professor with the Department of Electrical Engineering, Shanghai Jiao Tong University, Shanghai, China. His research interests include power system analysis and control, wind and PV power control and integration, and microgrids.

Muhammad Waseem Khan received the M.Sc. and Ph.D. degrees from Shanghai Jiao Tong University, Shanghai, China, in 2017 and 2020, respectively. He worked as a research and development software engineer with Yanfeng Automotive Trim Systems Company Ltd., Shanghai, and led different SAIC Volkswagen and Tesla projects. His research interests include multi-agent system, renewable power generations, and control and optimization techniques along with optimal and economical energy management strategies in micro grids.

Keyou Wang received the B.S. and M.S. degrees in electrical engineering from Shanghai Jiao Tong University, Shanghai, China, in 2001 and 2004, respectively, and the Ph.D. degree in electrical engineering from the Missouri S&T (formerly, University of Missouri-Rolla), Rolla, MO, USA, in 2008. He is currently a professor and the vice department chair of Electrical Engineering with Shanghai Jiao Tong University. His research interests include power system dynamic and stability, renewable energy integration, and converter dominated power systems. He serves as an associate editor for *IET Generation*, *Transmission and Distribution*.

Bei Han received her M.S. degree in electrical engineering from Shanghai Jiao Tong University, Shanghai, China, in 2009 and her Ph.D. in electrical engineering from Politecnico di Torino, Italy, in 2013. Currently, she is an assistant professor at Shanghai Jiao Tong University. Her research interests include complex power system modeling, data mining, and micro grids.

REFERENCES

[1] D. G. Wilson, R. D. Robinett, and G. Bacelli *et al.*, "Nonlinear WEC optimized geometric buoy design for efficient reactive power requirements," in *OCEANS 2019 MTS/IEEE SEATTLE*, Seattle, USA, 2019, pp. 1-6.

[2] A. Muetze and J. G. Vining, "Ocean wave energy conversion-a survey," in *Conference Record of the 2006 IEEE Industry Applications Conference Forty-First IAS Annual Meeting*, Tampa, USA, Oct. 2006, pp. 1410-1417.

[3] M. Noman, G. Li, and K. Wang *et al.*, "Electrical control strategy for an ocean energy conversion system," *Protection and Control of Modern Power Systems,* vol. 6, no. 2, pp. 1-18, Apr. 2021.

[4] D. Wang and K. Lu, "Design optimization of hydraulic energy storage and conversion system for wave energy converters," *Protection and Control of Modern Power Systems,* vol. 3, no. 1, pp. 1-9, Jan. 2018.

[5] Y. Zhang, T. Zeng, and Z. Gao, "Fault diagnosis and fault-tolerant control of energy maximization for wave energy converters," *IEEE Transactions on Sustainable Energy*, vol. 13, no. 3, pp. 1771-1778, May 2022.

[6] J. V. Ringwood, S. Zhan, and N. Faedo, "Empowering wave energy with control technology: possibilities and pitfalls," *Annual Reviews in Control*, vol. 55, pp. 18-44, Jan. 2023.

[7] Y. Hong, R. Waters, and C. Boström *et al.*, "Review on electrical control strategies for wave energy converting systems," *Renewable and Sustainable Energy Reviews,* vol. 31, pp. 329-342, Mar. 2014.

[8] X. Du, H. Chen, and C. Li *et al.*, "Wake galloping piezoelectric-electromagnetic hybrid ocean wave energy harvesting with oscillating water column," *Applied Energy*, vol. 353, Jan. 2024.

[9] A. Barua and M. S. Rasel, "Advances and challenges in ocean wave energy harvesting," *Sustainable Energy Technologies and Assessments*, vol. 61, Jan. 2024.

[10] A. T. Kotb, M. A. Nawar, and Y. A. Attai *et al.*, "Smart optimization algorithms to enhance an axial turbine performance for wave energy conversion," *Ocean Engineering*, vol. 291, Jan. 2024.

[11] S. K. Mishra, B. Appasani, and A. V. Jha *et al.*, "Centralized airflow control to reduce output power variation in a complex OWC ocean energy network," *Complexity*, vol. 2020, no. 1, Aug. 2020.

[12] J. Henriques, L. Gato, and A. D. O. Falcao *et al.*, "Latching control of a floating oscillating-water-column wave energy converter," *Renewable Energy*, vol. 90, pp. 229-241, May 2016.

[13] S. K. Mishra, S. Purwar, and N. Kishor, "An optimal and non-linear speed control of oscillating water column wave energy plant with wells turbine and DFIG," *International Journal of Renewable Energy Research*, vol. 6, no. 3, pp. 995-1006, Jun. 2016.

[14] S. K. Mishra, D. K. Mohanta, and B. Appasani *et al.*, "Overview of OWC mathematical model," in *OWC-Based Ocean Wave Energy Plants*, *Energy Systems in Electrical Engineering*, Berlin, Germany: Springer, Nov. 2021, pp. 15-27.

[15] B. Meghni, A. Saadoun, and Y. Amirat *et al.*, "Effective MPPT technique and robust power control of the PMSG wind turbine," *IEEJ Transactions on Electrical and Electronic Engineering*, vol. 10, no. 6, pp. 619-627, Nov. 2015.

[16] E. Shehata, "A comparative study of current control schemes for a direct-driven PMSG wind energy generation system," *Electric Power Systems Research*, vol. 143, pp. 197-205, Feb. 2017.

[17] R. Errouissi, A. Al-Durra, and M. Debouza, "A novel design of PI current controller for PMSG-based wind turbine considering transient performance specifications and control saturation," *IEEE Transactions on Industrial Electronics*, vol. 65, no. 11, pp. 8624-8634, Mar. 2018.

[18] R. E. Quintal-Palomo, M. Flota-Bañuelos, and A. Bassam *et al.*, "Post-fault demagnetization of a PMSG un-

der field oriented control operation," *IEEE Access,* vol. 9, pp. 53838-53848, Apr. 2021.

[19] P. Gajewski and K. Pieńkowski, "Direct Torque Control and Direct Power Control of wind turbine system with PMSG," *Przegląd Elektrotechniczny,* vol. 92, no. 10, pp. 249-253, Oct. 2016.

[20] Y. El Mourabit, A. Derouich, and A. El Ghzizal *et al.*, "Nonlinear backstepping control for PMSG wind turbine used on the real wind profile of the Dakhla-Morocco city," *International Transactions on Electrical Energy Systems*, vol. 30, no. 4, pp. 1-28, Apr. 2020.

[21] D. T. Gaebele, M. E. Magana, and T. K. Brekken *et al.*, "Second order sliding mode control of oscillating water column wave energy converters for power improvement," *IEEE Transactions on Sustainable Energy,* vol. 12, no. 2, pp. 1151-1160, Nov. 2020.

[22] T. Demonte Gonzalez, G. G. Parker, and E. Anderlini *et al.*, "Sliding mode control of a nonlinear wave energy converter model," *Journal of Marine Science and Engineering,* vol. 9, no. 9, Sept. 2021.

[23] A. Ghaedi, R. Sedaghati, and M. Mahmoudian *et al.*, "Reliability modeling of wave energy converters based on pelamis technology," *Electric Power Systems Research*, vol. 227, Feb. 2024.

[24] X. Bao, G. Huang, and M. Liu *et al.*, "Turbine fault diagnosis of the oscillating water column wave energy converter based on multi-lead residual neural networks," *Ocean Engineering*, vol. 291, Jan. 2024.

[25] R. H. Charlier and C. W. Finkl, "Poseidon to the rescue: mining the sea for energy—a sustainable extraction," in *Ocean Energy*: *Tide and Tidal Power*, Berlin, Germany: Springer, Feb. 2009, pp. 1-18.

[26] M. Alam, I. Kayes, and A. Hasan *et al.*, "Exploring SAARC's ocean energy potential: current status and future policies," *Energy Reports*, vol. 11, pp. 754-778, Jun. 2024.

[27] G. Chen and X. Cai, "Reconfigurable control for fault-tolerant of parallel converters in PMSG wind energy conversion system," *IEEE Transactions on Sustainable Energy*, vol. 10, no. 2, pp. 604-614, May 2018.

[28] M. Shahbazi, S. Saadate, and P. Poure *et al.*, "Open-circuit switch fault tolerant wind energy conversion system based on six/five-leg reconfigurable converter," *Electric Power Systems Research*, vol. 137, pp. 104-112, Aug. 2016.

[29] M. Shahbazi, M. R. Zolghadri, and P. Poure *et al.*, "Wind energy conversion system based on DFIG with open switch fault tolerant six-legs AC-DC-AC converter," in *IEEE International Conference on Industrial Technology (ICIT)*, Cape Town, South Africa, Feb. 2013, pp. 1656-1661.

[30] S. Karimi, A. Gaillard, and P. Poure *et al.*, "FPGA-based real-time power converter failure diagnosis for wind energy conversion systems," *IEEE Transactions on Industrial Electronics,* vol. 55, no. 12, pp. 4299-4308, Nov. 2008.

[31] M. Mahmoud, M. A. Abdelkareem, and A. G. Olabi, "Wave energy extraction technologies," in *Renewable Energy (volume 2)*: *Wave*, *Geothermal*, *and Bioenergy*, Amsterdam, Netherlands: Elsevier, pp. 37-51.

[32] S. A. Mortazavizadeh, R. Yazdanpanah, and D. C. Gaona *et al.*, "Fault diagnosis and condition monitoring in wave energy converters: a review," *Energies*, vol. 16, no. 19, Sept. 2023.

[33] A. Price, D. Campos-Gaona, and P. McCallum *et al.*, "HAPiWEC: towards a rapid prototyping rig for wave energy control co-design and testing," in *IEEE OCEANS 2023-Limerick*, Limerick, Ireland, Jun. 2023, pp. 1-9.

[34] S. Rasool, K. M. Muttaqi, and D. Sutanto, "A novel fault ride-through capability improvement scheme for the hybrid offshore wind-wave energy conversion systems," *Electric Power Systems Research*, vol. 217, Apr. 2023.

[35] D. Ramirez, M. Blanco, and M. E. Zarei *et al.*, "Robust control of a floating OWC WEC under open-switch fault condition in one or in both VSCs," *IET Renewable Power Generation,* vol. 14, no. 13, pp. 2538-2549, Oct. 2020.

[36] M. I. Marei, M. Mokhtar, and A. A. El-Sattar, "MPPT strategy based on speed control for AWS-based wave energy conversion system," *Renewable Energy*, vol. 83, pp. 305-317, Nov. 2015.

[37] P. E. Kakosimos and A. G. Kladas, "Implementation of photovoltaic array MPPT through fixed step predictive control technique," *Renewable energy*, vol. 36, no. 9, pp. 2508-2514, Sept. 2011.

[38] X. Yin and M. Lei, "Jointly improving energy efficiency and smoothing power oscillations of integrated offshore wind and photovoltaic power: a deep reinforcement learning approach," *Protection and Control of Modern Power Systems,* vol. 8, no. 2, pp. 1-11, Apr. 2023.

[39] G. Rajapakse, S. Jayasinghe, and A. Fleming *et al.*, "Grid integration and power smoothing of an oscillating water column wave energy converter," *Energies*, vol. 11, no. 7, Jul. 2018.

[40] R. Matar, N. Abcha, and I. Abroug *et al.*, "A multi-approach analysis for monitoring wave energy driven by coastal extremes," *Water*, vol. 16, no. 8, Apr. 2024.

[41] A. S. Shehata, Q. Xiao, and K. M. Saqr *et al.*, "Wells turbine for wave energy conversion: a review," *International Journal of Energy Research*, vol. 41, no. 1, pp. 6-38, Jan. 2017.

[42] J. Lekube, A. J. Garrido, and I. Garrido *et al.*, "Flow control in wells turbines for harnessing maximum wave power," *Sensors*, vol. 18, no. 2, Feb. 2018.

[43] H.-S. Ko, "Modeling and control of PMSG-based variable-speed wind turbine," *Wind Turbine Control and Monitoring*, vol. 80, no. 1, pp. 3-21, Jan. 2014.

[44] A. Uphues, K. Nötzold, and R. Wegener *et al.*, "PR-controller in a 2 MW grid side wind power converter," in *2012 IEEE International Conference on Industrial Technology*, Athens, Greece, Mar. 2012, pp. 1073-1078.

[45] O. A. AlKawak, J. R. R. Kumar, and S. S. Daniel *et al.*, "Hybrid method based energy management of electric vehicles using battery-super capacitor energy storage," *Journal of Energy Storage*, vol. 77, Jan. 2024.

[46] R. Saifulin, T. Pajchrowski, and I. Breido, "A buffer power source based on a supercapacitor for starting an induction motor under load," *Energies*, vol. 14, no. 16, Aug. 2021.

[47] A. Pirooz and R. Noroozian, "Model predictive control of classic bidirectional DC-DC converter for battery applications," in *2016 7th Power Electronics and Drive Systems Technologies Conference (PEDSTC)*, Tehran, Iran, Feb. 2016, pp. 517-522.